The Volyn biota (Ukraine) – 1.5 Ga old (micro)fossils in 3D-preservation, a spotlight on the 'boring billion'

Gerhard Franz[1], Vladimir Khomenko[2], Peter Lyckberg[3], Vsevolod Chournousenko[4], Ulrich Struck[5], Ulrich Gernert[6], Jörg Nissen[6]

[1]Institut für Angewandte Geowissenschaften, Technische Universität Berlin, D-10587 Berlin, Germany

[2]M.P. Semenenko Institute of Geochemistry, Mineralogy and Ore Formation, The National Academy of Sciences of Ukraine, 34, Palladina av., Kyiv, 03142, Ukraine

[3]Luxembourg National Museum of Natural History, 25 Rue Münster, 2160 Luxembourg, Luxembourg

[4]Volyn Quartz Samotsvety Company, Khoroshiv (Volodarsk-Volynski), Ukraine

[5]Museum für Naturkunde, Leibniz-Institut für Evolutions- und Biodiversitätsforschung, Invalidenstraße 43, Berlin, D-10115, Germany

[6]Zentraleinrichtung Elektronenmikroskopie, Technische Universität Berlin, D-10623 Berlin, Germany

Correspondence to: Gerhard Franz (gefra548@gmail.com; gerhard.franz@tu-berlin.de)

Abstract

The Volyn biota, fossilized organisms with a minimum age of 1.5 Ga, were found in cavities in granitic pegmatites from the Korosten pluton, NW Ukrainian shield. Fossilization was due to influx of hydrothermal fluorine-rich waters, which silicified the outermost part of the organisms, thus preserving the 3D morphology. Details of the morphology (investigated by scanning electron microscopy) show that the majority of the specimens is filamentous, of a large variety with diameters ranging from ~10 μm to ~200 μm, thin filaments with typical branching, thick filaments with ball-shaped outgrowths and dented surface. Filaments can be straight or conical, curvilinear or strongly curved, up to mm in length, some with a central channel. Some filaments show indications for segmentation, are grown as sessile organisms onto substrate; others show both intact ends, indicating growth in soft medium or floating in water. Objects with flaky morphology and agglutinating filaments are interpreted as fossil biofilms. Other objects are hollow and show a large variety of forms; spherical objects are scarce. Infrared spectroscopy indicates the presence of chitosan in one filament, electron microprobe analysis of nm-sized inclusions in filaments identified the presence of Bi(Te,S)

35   minerals, and both observations are compatible with the interpretation of filaments as fungi-

36   like organisms. Stable C- and N-isotope data of bulk samples are in the range of -31 to -47 ‰

37   $\delta^{13}C/^{12}C$, and of +3 to +10 ‰ $\delta^{15}N/^{14}N$, indicating possible methanogenic bacteria as part of

38   the subsurface micro-ecosystem. The Volyn biota show that at 1.5 Ga fungi-like organisms

39   lived in the continental deep biosphere, where complex forms of life existed, well above the

40   microscopic level.

41

42

43   **1 Introduction**

44   Precambrian fossils are generally not well preserved because of the absence of skeletal parts.

45   In addition, most Precambrian fossil record is from sedimentary rocks with strong diagenetic

46   or even metamorphic overprint, which destroyed much of the original morphology and in

47   extreme cases of very old organisms left only an isotopic signature (e.g. Alleon et al., 2018;

48   Berbee et al., 2020). Therefore, their biogenicity is often disputed especially when the organic

49   matter (OM) is completely replaced, often by silica or pyrite. A preservation of 3D-morphology

50   is very rare and requires special fossilization conditions, which include first prevention of rapid

51   decay of the OM and then preservation of the space around the fossil in order to preserve its

52   original morphology. These conditions were fulfilled in pegmatites of the Volyn pegmatite

53   field, Ukraine, associated with the Korosten Pluton. These so-called 'chamber pegmatites'

54   contain large miarolitic cavities in which OM named (oxy)-kerite was found and in previous

55   investigations interpreted as an example of a-biogenic formation (Ginzburg et al., 1987;

56   Luk'yanova et al., 1992), later re-interpreted as fossil cyanobacteria (Gorlenko et al., 2000;

57   Zhmur, 2003) from a geyser type deposit. Ginzburg et al. (1987) give a composition of 60-76

58   wt% C, 5-7 wt% H, 9-23 wt% O, 8-9 wt% N, and 2-3 wt% S and an empirical formula of

59   $C_{491}H_{386}O_{87}(S)N$. Gorlenko et al. (2000) and Zhmur (2003) mention masses of up to 3 kg of

60   kerite in one of the cavities with an irregular distribution within the pegmatite.

61   The organisms lived in these cavities and provide an example of the Precambrian deep

62   biosphere. Their fossilization conditions included sudden influx of hot hydrothermal waters in

63   the geyser system, where magmatic fluids rich in SiF_4 mixed with meteoric waters (Franz et al.,

64   2022a), infiltration of Si-Al into the outermost layer of the fossils, and formation of dominantly

65   clay mineral encrustations. The 1.76 Ga intrusion age of the pegmatites (U-Pb zircon;

66   Shumlyanskyy et al., 2021) provides a maximum age of the fossils; the minimum age of 1.5 Ga

67   is provided by the age of formation of a breccia, which contains degraded OM, opal with OM,

68   buddingtonite which NH_4-content was provided by the degraded OM, and muscovite ($^{40}Ar-^{39}Ar$

69   laser ablation data; Franz et al., 2022b). Although some of the miarolitic chambers collapsed,

70   producing the muscovite-bearing breccia, other chambers are still intact and were mined since

71   the 1930ies for piezo quartz and until now for pegmatite minerals such as beryl and topaz

72   (Ivanovich and Alekseevich, 2007; Lyckberg et al., 2009, 2019).

73   We report here details about the morphology and the internal structure of the fossils,

74   investigated by scanning electron microscopy (SEM) and electron microprobe analysis

75   (EMPA), and provide stable C-N isotope and infrared spectroscopy (FTIR) data, which allow

76   speculating about the types of organisms. An important point is that these 'micro'-fossils in

77   many cases reach a size well above the microscopic level, with filaments of several mm in

78   length. The age of the fossils of 1.5 Ga in the middle of the 'boring billion' and gives insight

79   into the organisms of the deep biosphere.

80
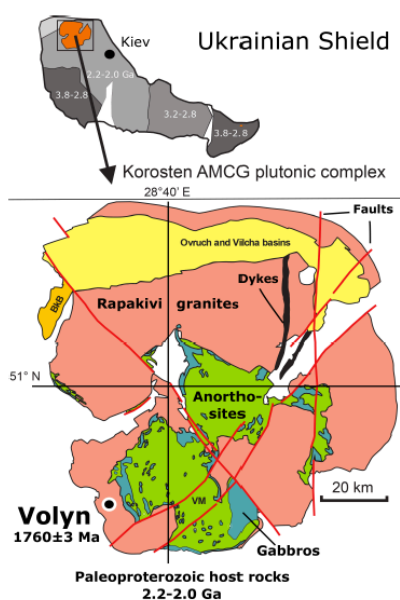
Fig. 1 Location of the Volyn pegmatite field in the Ukrainian shield, which hosts the Volyn biota (reproduced from Franz et al., 2022a)

2 Geological framework and sample material

85   The locality in the Ukrainian Precambrian shield is associated with the Korosten anorthosite-

86   mangerite-charnockite-granite plutonic complex (Shumlyanksyy et al., 2012) (Fig. 1). The

87   samples were recovered from underground in shaft 3 of the mine from a depth of approximately

88   100 m, one sample was obtained from the mineralogical museum of the Academy of Sciences,

89   Kiev, and one beryl sample with kerite on beryl was collected from the mine tailings (Table 1).

90   Two additional samples of topaz from the museum in Kiev with kerite (Fig. 2) were not

91   investigated in detail. The samples from underground could be simply picked up with no need
92   for separation from rock matrix and were stored in plastic sample bags.

93
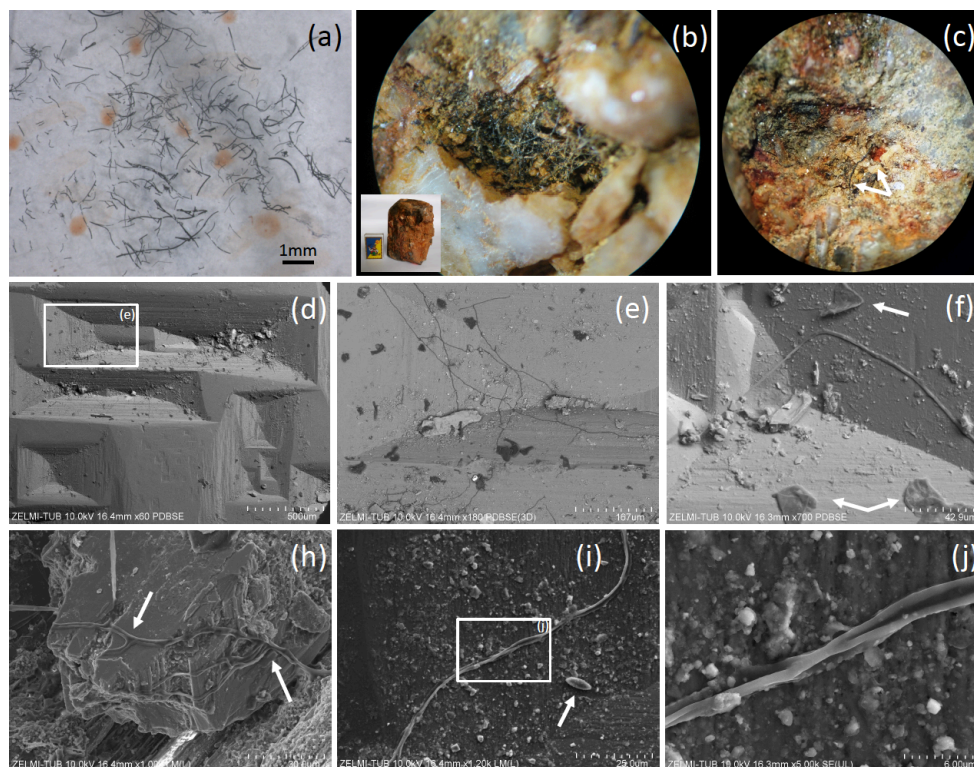
Fig. 2 (a) Photograph of sample #0, illustrating the pieces of broken, solitary kerite filaments of mm-length. (b) Photograph of kerite filaments on topaz (white crystals with Fe-oxide-hydroxide staining; inset shows topaz crystal with 5-cm large matchbox for scale, image diameter approximately 2 mm). (c) Filaments of different diameter on topaz (arrows; image diameter approximately 3 mm). (d) SEM image (with combined back scattered mode) of beryl prism surface with characteristic etch pits. Rectangle indicates position of (e), which shows filamentous kerite together with kerite in irregular shape (dark contrast indicates organic matter). (f) SEM image, arrows point to kerite with irregular shape. (h) Kerite filaments with branching (arrows) in dissolution feature of beryl. (i) Kerite filament and spherical kerite (arrow) in an etch pit of beryl; rectangle indicates position of (j), illustrating the irregular diameter of the filament.

106

107   The sample #0 consists of broken filaments of several mm length (Fig. 2a) and it is likely that

108   the original length was much larger on the cm scale. It was also found grown onto a topaz

109   crystal (Fig. 2b, c). On beryl it was found attached to dissolution features on the surface of the

110   crystals, but not only in the common filamentous form, but also in irregular shape (Fig. 2d-j)

111   and rarely in spherical shape (Fig. 2i). Although the previous reports mention mostly filaments

112 with smooth surface, our new observations revealed a large variety of different types of

113 filaments, described below.

3 Methods

115 The samples were investigated by SEM and EMPA. SEM images were obtained with a Hitachi

116 SU8030 instrument, equipped with an EDAX EDS system with a 30 mm^2 silicon drift detector

117 (SDD) fitted with a silicon nitride window. Samples were coated with an approximately 5 nm

118 thick Ir layer allowing for high-resolution imaging of the filaments' surfaces without the

119 structure of commonly applied Au coating. The kerite samples without further cleaning or

120 preparation were mounted on Al stubs stickered with conductive carbon tabs. The beryl crystals

121 with kerite filaments were dust-cleaned with compressed air and coated with C.

122

123 Table 1: List of samples

No./GFZ no.	Year of sampling	Material	Location
0/Museum Ac. Sci. Kyiv	unknown	kerite	unknown
1/G017809	2018	kerite	shaft 3
2/G017810	2018	kerite	shaft 3
3/G017811	2018	kerite	shaft 3
4/G017812	2018	kerite	shaft 3
5/G017813	2013	kerite	shaft 3
6/G017814	2013	kerite	shaft 3
7/G017815	2013	kerite	shaft 3
2008-V-10	2008	beryl crystal with etch pits	mine tailings pegmatite #2

124

125 The JEOL JXA-8530F field emission electron microprobe at TU Berlin was used to investigate

126 mounts embedded in epoxy, but with C-coating, for quantitative results and less absorbance

127 (compared to Ir). EPMA data for element distribution maps of cross sections or of parts of the

128 rim of the filaments and flaky kerite were acquired in the wave-length dispersive mode using

129 an 8 kV, 20 nA beam with a probe diameter of 64 nm. Back-scattered electron images (BSE)

130 were taken to select appropriate sites. Mappings were done in stage scan-modus with pixel

131 resolution between 277 and 360 x 180 and 265, with a pixel size of mostly 80 nm, and a dwell

132 time per pixel of 200 ms. Total scan areas varied between 70 x 36 μm to 33.2 x 31.8 μm.

133 Stable isotope analysis and concentration measurements of nitrogen and carbon were performed

134 simultaneously with a THERMO/Finnigan MAT V isotope ratio mass spectrometer, coupled to

135 a THERMO Flash EA 1112 elemental analyzer via a THERMO/Finnigan Conflo IV- interface

136   in the stable isotope laboratory of the Museum für Naturkunde, Berlin. Isotope ratios are

137   expressed in the conventional delta notation (δ^{13}C / δ^{15}N) relative to atmospheric N (Mariotti,

138   1983) and VPDB (Vienna PeeDee Belemnite standard). Standard deviation for repeated

139   measurements of lab standard material (peptone) is generally better than 0.15 per mill (‰) for

140   both N and C. Standard deviations of concentration measurements of replicates of our lab

141   standard are <3% of the concentration analyzed.

142   FTIR absorption spectra of several small, 40-60 µm wide, translucent dark-brown fragments of

143   kerite (sample #0, which showed the least mineralization crust) were measured in the spectral

144   range 7000 – 700 cm^{-1} at room temperature using a Bruker IFS 66 spectrometer equipped with

145   an IR-microscope. The kerite fragments were selected under a binocular microscope and placed

146   on an IR-transparent KBr plate. Spectra were taken in the transmittance mode at a spectral

147   resolution of 4 cm^{-1} with a measuring spot diameter of 40 µm. The reference spectra were

148   measured through the same KBr plate. The time-averaged signal was collected over 200 scans

149   in both reference and sample spectra. For comparison, absorption spectra of chitin (poly-(1,4)-

150   β-N-acetyl-D-glucosamine) and >75% deacetylated chitin, or chitosan (2-amino-2-deoxy-

151   (1,4)-β-D-glucopyranan, both produced by Sigma-Aldrich Chemie GmbH (C7170-100G,

152   C3646-10G) from shrimp shells, were measured in several single flattened, 30-50 microns thick

153   transparent flakes of these materials at the same conditions. Band assignments are based on

154   literature comparison (Table 1 Supplement).

155   **4 Results**

156   **4.1 Morphology**

157   **4.1.1 Filaments**

158   Filaments are curvilinear with smooth surfaces and circular cross section (Fig. 3) with different

159   types of ends (Fig. 4). Other types have a structured surface, some are conical, others strongly

160   curved (Figs. 5, 6). Branching is typical for filaments with smooth surface, and was observed

161   as Y-, T-, and double-T-branching (Fig. 3b, h), as multiple branching (Fig. 3c), and combined

162   Y-T-branching (Fig. 3d). Clear indications for anastomosing filaments were not found. Multiple

163   branching represents the beginning of growth of filaments (Fig. 3e). In others, globular

164   outgrowths possibly mark the beginning of new branches (Fig. 3g). Whereas the diameter of

165   the individual filaments can be homogeneous between approximately 10 µm and 20 µm (sample

166   #0), others (e.g. sample #3; Fig. 3f) show different diameters, between a few µm and several

167   tens of µm. Ball-shaped outgrowths at the end of a filament occur together with a conical

168   thinning-out filament (sample #1; Fig. 3i). Conical, thinning out filaments originate in Y-

169   branching from a thicker filament with constant diameter (Fig. 3m). One object was identified

with multiple conical filaments, with claw-like curved ends (sample #6; Fig. 3j, k, l). The bottom part can be interpreted as beginning of growth of the filaments on a substrate, i.e. the clay mineral assemblage in the miarolitic cavities.

Most filaments are broken pieces of larger filaments, and preserved length is in the order of mm, and it can be assumed that the original length was up to cm. Complete filaments were observed, with one end ball-shaped, the other end thinning out (Fig. 6i, o). Whereas beginning of a filament is rarely observed, ends are frequently preserved (Fig. 4) and can be either simply round (Fig. 4a), ball-shaped (Fig. 4b-f), rarely with oval shape (Fig. 4e), or conical-thinning out (Fig. 4g, l, m).
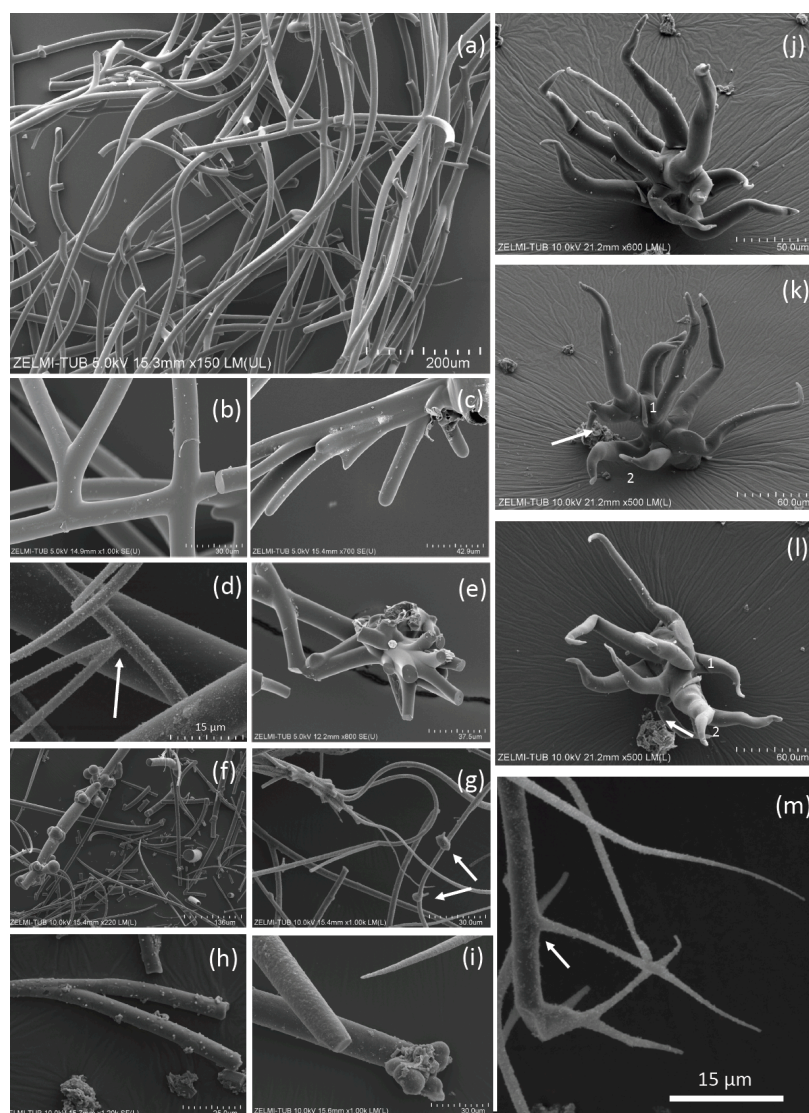
180 **Fig. 3 SEM images of curvilinear filaments with smooth surfaces and circular cross**
181 **section. (a) Overview of sample #0, illustrating the amount of material with homogeneous**
182 **diameter of approximately 10 μm, length of more than 1 cm, round ends. (b) Branching**
183 **with Y-, T- and double-T-junctions. (c) Multiple branching and (d) combined Y- and T-**
184 **branching. (e) Possible multiple branching representing the beginning of the filaments. (f)**
185 **Overview (sample #3) with filaments of variable diameter and (g) multiple branching**
186 **(upper left) and small outgrowths (arrows). (h) Sample #4 with Y-branching. (i) Sample**
187 **#1 showing 3 filaments, one thinning out (upper left), one with constant diameter with**
188 **ball-shaped outgrowths on end (below), and a slightly conical one (above). (j, k, l) Image**
189 **of multiple, conical filaments with claw-like ends, growing from a common center; view**
190 **of the same object (sample #6) in different perspectives. In (k) and (l) numbers 1 and 2**
191 **identify the same beginning and end of a filament; arrows point to a fluorite crystal. (m)**
192 **Y-branching of a thinning-out filament (arrow) starting from a filament with constant**
193 **thickness. The star-like shape in the center is not branching, it shows different filaments**
194 **in different heights.**

195

196 Ball-shaped outgrowths (Fig. 4h) and multiple ball-shaped ends (Fig. 4i) possibly mark the

197 beginning of new branches, and balls can be situated asymmetrically at the end of a filament

198 (Fig. 4j). The structured surface of this ball-shaped end is caused by the fossilization process,

199 as indicated by the round pores in the surface, together with mineral incrustations (Fig. 4k).

200 This is also seen on the surface of a 300 μm long conical filament fragment (Fig. 4m, n), which

201 has a μm-wide rim of mineral incrustations with a homogeneous interior part (Fig. 4o).

202 The structured surface is only partly a result of the fossilization process. Figure 5a-f shows a

203 filament with approximately 4 mm preserved length and oval cross section (120x80 μm thick

204 on one end), which has a dented surface and bulbous outgrowths (Fig. 4d). Another example of

205 a strongly curved filament (Fig. 4g-l) with bulbous surface, several mm in length and near to

206 200 μm diameter shows irregular segmentation in distances between 35 μm and 70 μm. On the

207 surface of the filament, relicts of a sheath are visible, partly the sheath is intact. The transition

208 between the intact sheath and the remnants exhibits a polygonal structure and circular 1-2 μm

209 wide holes, probably caused by decay/fossilization. Segmentation is also seen in a branched

210 filament with approximately 3-5 μm wide ridges (Fig. 4m, n, o). This filament has a mineralized

211 outer part of clay minerals with irregular ridges; however, where branching starts, the surface

212 is intact. We interpret these irregular ridges as irregular segmentation of the filament,

213 accentuated and emphasized by fossilization.

214 Some samples have joint occurrence of filaments with smooth, slightly, and strongly bulbous

215 surfaces (Fig. 6a, b), and joint occurrence of straight, slightly, and strongly curved filaments

216 with irregular segmentation (Fig. 6c, d). The strongly bulbous filaments are transitional to

217 outgrowths (Fig. 6d). Segmentation is indicated (Fig. 6e) and the surface can be strongly

218 sculptured. The filaments have variable diameters from 75 μm (Fig. 6e) to approximately 250

219   µm (Fig. 6d, f). Some thin filaments show clear indication for segmentation (Fig. 6g, h). The
220   strongly sculptured surface consists of small ball-shaped outgrowths. Joint occurrence of
221   filaments with strongly sculptured surface and smooth surface and with slight striation
222   perpendicular to filament length, and filaments with strong sculptured surface (Fig. 6k, l, m, n),
223   indicates that these are probably different types of organisms, not different stages of
224   fossilization.

225
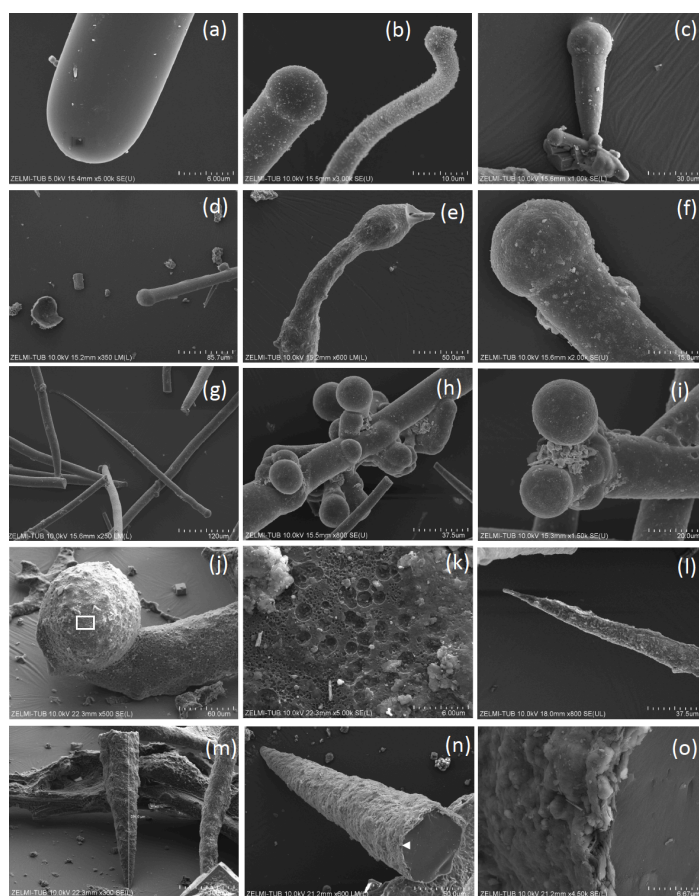
Fig. 4 SEM images of ends of filaments with smooth surface. (a) Simple round end (sample #0). (b) Ball-shaped end of straight and curved filament (sample #3). (c) Ball-shaped end of conical filament (sample #1). (d) Ball-shaped end of straight filament (sample #5). (e) Oval-shaped outgrowths near end of filament (sample #7). (f) Ball-shaped end (sample #1). (g) Complete filament with one end thinning out, one with a round end (sample #1). (h) Ball-shaped outgrowths and ends (sample #3). (i) Double ball at end of filament (sample #1) (j) Ball-shaped end; rectangle indicates position of (k), surface of the ball with mineral incrustations and porosity, interpreted as result of decay/fossilization (sample #6). (l) Thinning-out of a filament (sample #5). (m, n) Cone-shaped filament in different perspective, approximately 300 µm preserved length (sample #6); white rectangle indicates position of (o) detail of the 1-2 µm wide rim with mineral incrustations.

237
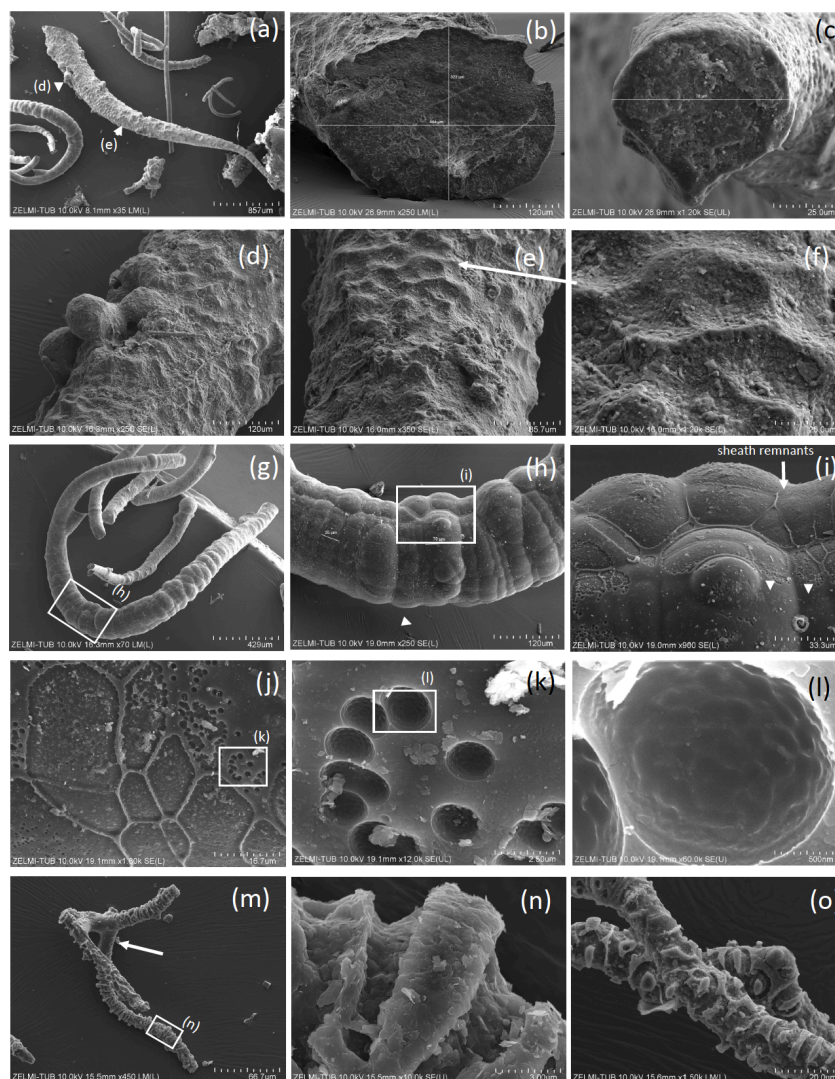
9

Fig. 5 Filaments with structured, rough surface. (a) Conical filament of approximately 4 mm preserved length, upper oval diameter (b) 440 µm x 320 µm, (c) thin end 70 µm (sample #5); triangles point to details shown in (d), bulbous outgrowths, and (e, f) dented surface. (g) Strongly curved filament with bulbous surface, several mm in length and near to 200 µm diameter (sample #5). Rectangle shows position of (h), bulbous surface with irregular segmentation in distances between 35 µm and 70 µm; rectangle indicates position of (i), white triangle to position of (j). (i) In the upper part of the filament, relicts of a sheath are visible (single arrow), in the lower part the sheath is intact (triangles point to the contact). (j) The transition between the intact sheath and the remnants in the lower part of the filament exhibits a polygonal structure and (k, l) circular 1-2 µm wide holes, probably caused by decay/fossilization. (m) Branched filament with approximately 3-5 µm wide ridges (sample #2). Note intact surface where branching starts (arrow). (n) Detail of central part of (m). Platy objects are clay minerals. (o) Similar feature of filament surface (sample #4) with irregular ridges, indicating irregular segmentation.

254
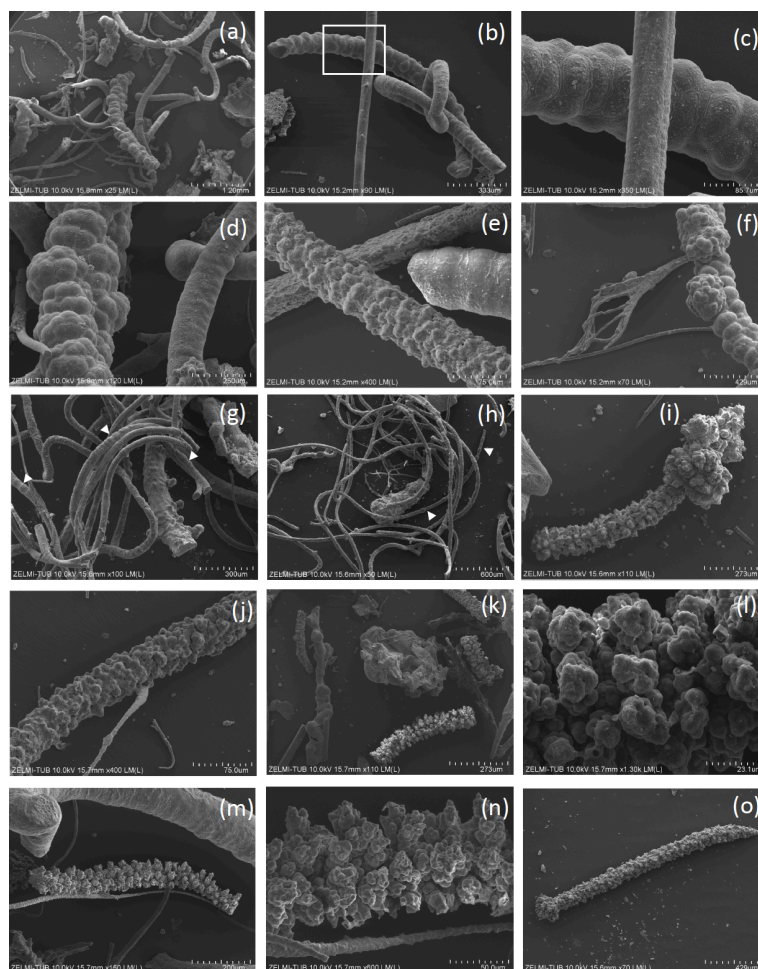
Fig. 6 SEM images of filaments with structured, rough surface 2. (a) Overview illustrating joint occurrence of smooth, slightly, and strongly bulbous surfaces (sample #5). (b) Joint occurrence of straight, slightly and strongly curved filaments; rectangle indicates detail in (c) with irregular segmentation of the slightly curved filament. The straight filament also shows a slight structure on the surface (lower right). (d) Joint occurrence of slightly bulbous (right) and strongly bulbous filaments, transitional to outgrowths. (e) Filament with indication for segmentation (right) and filament with strongly sculptured surface; note small diameter (75 µm) compared to the large filament in (d). (f) Thick filament with bulbous outgrowths, next to thin agglutinated filaments. (g, h) Thin filaments with indication for segmentation (white triangles). (i) Complete filament of approximately 1 mm length with strongly sculptured surface and outgrowths. (j) Part of a filament with strongly sculptured surface. (k) Joint occurrence of filaments with strongly sculptured surface and smooth surface, together with and irregularly shaped object (center). (l) Detail of strongly sculptured surface, which consists of small ball-shaped outgrowths. Note fluorite crystal in upper right, below label (m), which shows joint occurrence of thick filament (top) with slight striation perpendicular to filament length, and filament with strong sculptured surface, detail shown in (n). (o) Almost 2 mm long complete filament, one thin end, one with outgrowths.

273

4.1.2 Hollow objects

275 Some objects appear hollow (Fig. 7); one object (Fig. 7a, b) has a hollow lower part transitional
276 into a more solid upper, strongly bulbous part. The hollow rather irregular objects (Fig. 7c)
277 occur together with filaments. Filaments can be also hollow (Fig. 7d-h) and the thickness of the
278 outer rim is approximately 2 μm (Fig. 7h). This is the width of the fossilized outer part of
279 filaments, which we documented in the previous study (Franz et al., 2022a) and therefore we
280 interpret the hollow objects as organisms in which the interior part was completely decayed
281 during and after the fossilization process. Some of the hollow objects are bowl-shaped (Fig. 7i-
282 n). One such object (Fig. 8) is >1 mm large and from the view in different perspectives is can
283 be seen that it is grown onto mineral substrate; next to the clay minerals fluorite is a
284 characteristic mineral and indicates a high fluorine activity in the fossilizing fluid (Franz et al.,
285 2022a). The base of mineral substrate is followed by an approximately 10 μm thick solid rim
286 with bulbous outgrowths.
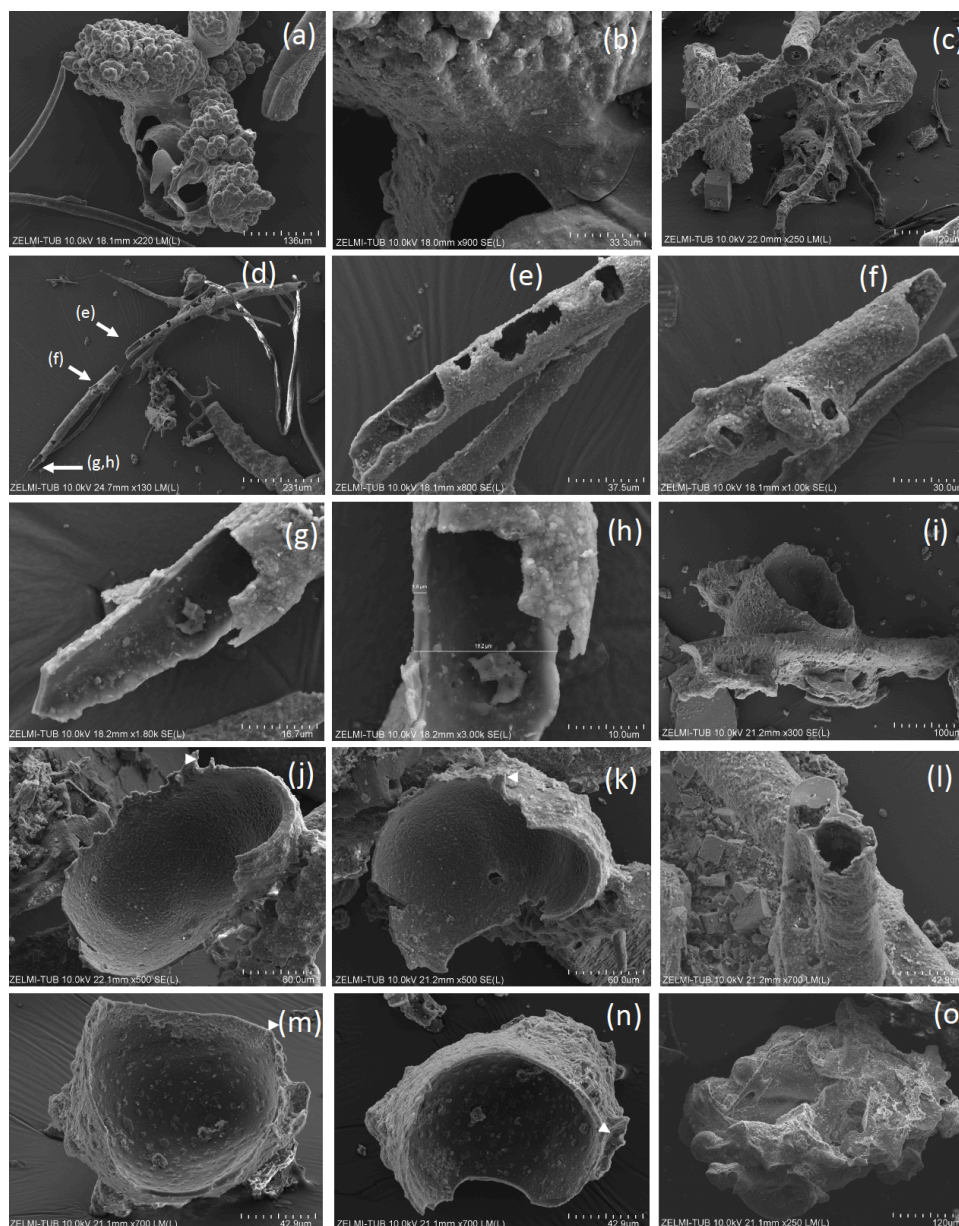
Fig. 7 SEM images of hollow objects. (a) Irregular-bulbous base of a strongly sculptured object, with (b) detail of the transition (center in (a); sample #5). (c) Irregular hollow object below filaments (sample #6). (d) Hollow filament, approximately 1 mm preserved length; position of enlarged parts in (e-h) is indicated (sample #5). The mineralized rim is 1-2 μm wide, diameter near 20 μm. (f) Bulbous outgrowths are also hollow. (i) Filament with an attached hollow form, similar to outgrowths, but much larger (sample #6). (j, k) Same object as in (i), enlarged in two different perspectives; white triangle indicates identical point. (l) Hollow filament next to a filament with a central channel (sample #6). (m, n) Isolated hollow bowl-shaped object in two different perspectives; white triangle indicates identical point (sample #6). (o) Irregular object, partly hollow (sample #6).

13

298
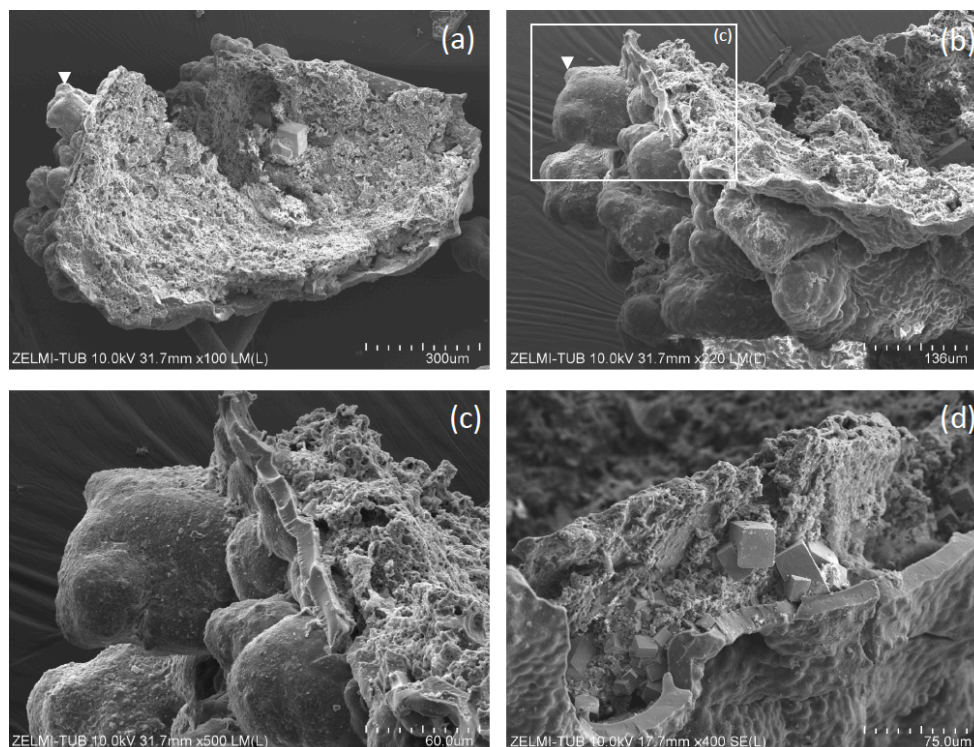
299

Fig. 8 SEM images of >1 mm large bowl-shaped object (sample #5) (a) seen from below, grown onto mineral substrate; euhedral crystal is fluorite, white triangle indicates position of (b), enlarged part of the rim. Rectangle indicates position of (c) illustrating the base of mineral substrate (right) followed by an approximately 10 µm thick solid rim with bulbous outgrowths. (d) Detail of the solid rim with several fluorite crystals.

305

4.1.3 Spherical objects

Most spherical objects (Fig. 9) appear as rather complete, with only some parts broken off. One object with a double-ball shape (Fig. 9a,b) is clearly grown onto the substrate (Fig. 9c). The double-ball with remnants of a sheath points to cell separation. Note the different size of the objects from < 10 µm (Fig. 9m) to > 1 mm (Fig. 9g). Two small objects identified on the etched beryl surface appear like seeds or spores (Fig. 9l, m).

312
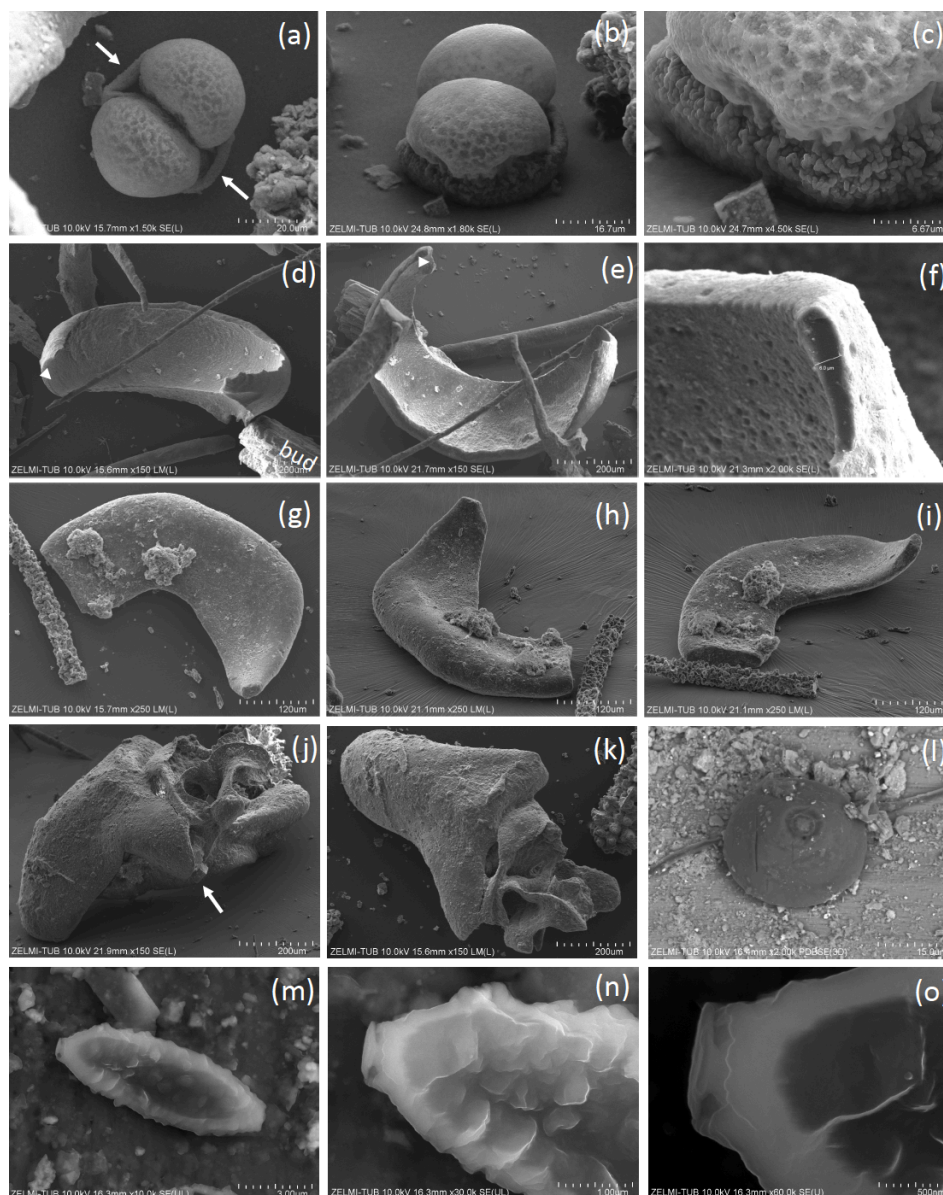
Fig. 9 SEM images of spherical objects. (a, b, c) Same object in different perspective and magnification; arrows in (a) point to a sheath; the euhedral crystal in (c) is fluorite. The object growth from a flat mineral surface into a double-ball with dented surface. (d, e) Same object in different orientation; white triangle indicates identical position; bud = buddingtonite. (c) The thickness measured at one point is approximately 6 µm. (g, h, i) Approximately 0.5 mm large object in different perspective with mineral incrustations. (j, k) Irregular, partly hollow object in different perspective. (l) Perfectly round object, sitting on a filament, on etched surface of beryl (compare Fig. 2d); the circular round structure on its top is beam damage. (m, n, o) Oval object on etched surface on beryl (compare Fig. 2i). The lower contrast (dark) in the central part indicates less dense (partly hollow) material.

4.1.4 Irregular objects

Irregular, flaky objects are abundant, especially on the surface of the beryl crystal (Fig. 2e, f), but also in many samples (e.g. Fig. 6k, 7a, c, o, 8, 9j, k). They show the same fossilization features as the filaments with a thin rim enriched in Si, Al, Ca, and P, loss of N, and oxygenation (Franz et al., 2022a). In some samples (Fig. 6f) filaments appear agglutinated by OM and we interpret these as well as the irregular objects on the beryl crystals as fossilized biofilm.

4.2 Internal structure

For investigation of the internal structure we used SEM images of broken filaments and other objects, as well as polished sections embedded in epoxy, investigated by BSE images including mapping of element distribution. Data of open-pyrolysis and TEM data (Franz et al., 2022a) had shown that the OM is highly mature, amorphous oxy-kerite. Indications for an outer cell wall are absent, because the outer rim of the fossils is silicified, partly with formation of mineral incrustations.

Segmentation of filaments, which might be a characteristic phenomenon for certain organisms and is observed in the filaments' morphology (Figs. 5g, h, 6b, c, e, h) is not obvious in cross section, but one section shows internal cracks, separating the filament in ~50 μm to 100 μm wide segments (Fig. 10a, b). A section of a bulbous fossil shows cracks, which separate the individual bulbs from each other (Fig. 10g, h).

The outer rim of the filament shows the typical enrichment of Si and Al (Fig. 10b), and the inner, homogenous and not silicified part shows abundant, nm-sized mineral inclusions (Fig. 10c). They are located in the central part and thus not related to the fossilization process, irregularly distributed or in linear array of several crystals (Fig. 10e, h). The minerals were analyzed with the EDS-system and due to their small size in the order of a few nanometers,

348
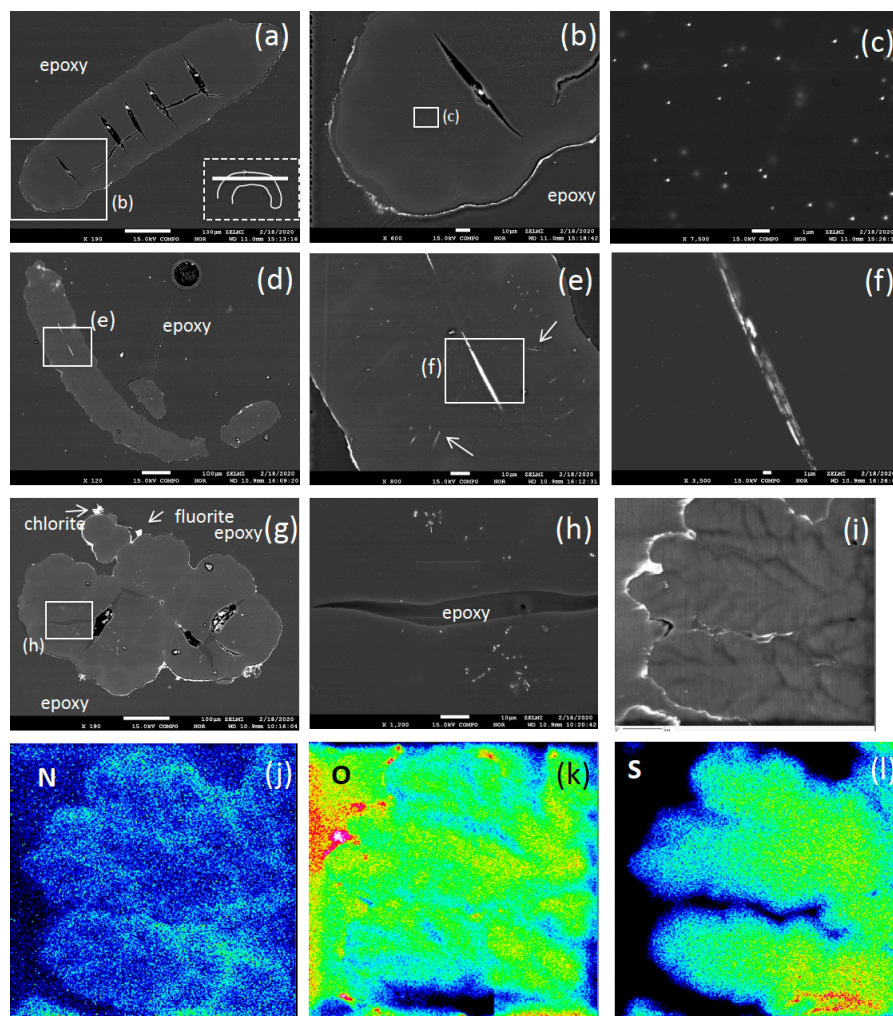
Fig. 10: BSE images of filamentous (a-f) and bulbous fossils (g, h, i), embedded in epoxy, polished thin section and element distribution (j, k, l). (a) Part of curved filament; orientation of section is shown in rectangle (dashed lines), position of enlargement (b) in rectangle (solid lines). Open cracks (black contrast, with impurities from polishing material) indicate approximately 50 μm to 100 μm wide segments. (b) Silicified outer rim (white contrast, irregular) and a narrow, up to 10 μm wide inner rim, are interpreted as effect of fossilization. The homogeneous appearing central part shows in the enlarged image (c) irregularly distributed inclusions, tens of nm in size, of Bi-S-Te minerals. (d) Filament with two, central oriented Bi-S-Te mineral inclusions, approximately 50 μm in length and 1-2 μm wide, enlarged shown in (e) and (f). Arrows in (e) point to straight aligned inclusions, and (f) shows irregular contrast, possibly caused by heterogeneous distribution of Fe and Cu in the Bi-S-Te minerals. (g) Bulbous fossil, with silicified rim and encrustations of chlorite and fluorite. Cracks, partly filled with epoxy, separate individual bulbs from each other. (h) Enlarged part showing irregularly distributed and aligned nm-sized Bi-S-Te mineral inclusions, and epoxy-filled crack. (i) Bulbous fossil with element distribution of N (j), O (k), and S (l), indicating an interior structure with possible former cell walls.

366　much smaller than the excitation volume of the electron beam, only mixed analyses with the

367　organic material could be obtained (Table 2). Recalculation of the analyses without the organic

368　compounds C, O, and N yielded an atomic ratio of Bi:(S,Te) near 1:1, indicating minerals such

369　as ingodite Bi(S,Te) or joseite $Bi_4(S,Te)_3$.The example of the bulbous filament (Fig. 10g) with

370　inclusions also shows a Bi(S,Te) mineral, located in the central part. The heterogenous BSE

371　contrast is caused by different trace compounds of Fe and Cu. Element distribution of N and O

372　(Fig., 10j, k) in a bulbous fossil, indicated by different BSE contrast (Fig. 10i), show an internal

373　structure, possibly indicating a primary separation into different cells, whereas S (Fig. 10l)

374　shows a systematic decrease towards the rims of the object, as a result of decay and/or

375　fossilization.

376

377　Table 2 EDS analyses of Bi-sulfide-telluride inclusions

Analysis#	15 06[1]	13 03[2]	13[3] n=18	Min-max
S atom%	0.27	2.59	0.20	n.d. – 0.52
Te	0.13	0.06	0.12	n.d. – 0.51
Bi	0.29	2.05	0.24	0.01-0.68
Pb	0.03	n.d.	n.d.	
Fe	n.d.	0.19	n.d.	
Cu	n.d.	0.22	n.d.	
C	86.24	84.86	83.38	80.19-96.15
N	5.91	4.89	3.16	n.d.-7.18
O	7.13	5.14	10.12	2.74-15.78
Sum[4]	100	100	100	
recalculated	15 06	13 03	13 n=19	Min-max
S atom%	38	51	37	3-55
Te	18	1	25	1-90
Bi	40	40	46	7-68
Pb	4	0		
Fe		4		
Cu		4		
Sum	100	100	100	

378　[1] Fig. 10h; [2] Fig. 10f inclusion in channel; [3] average of 18 analyses, inclusions in matrix, Fig.

379　10b,c; [4] normalized; n.d. = not detected

380

381

382
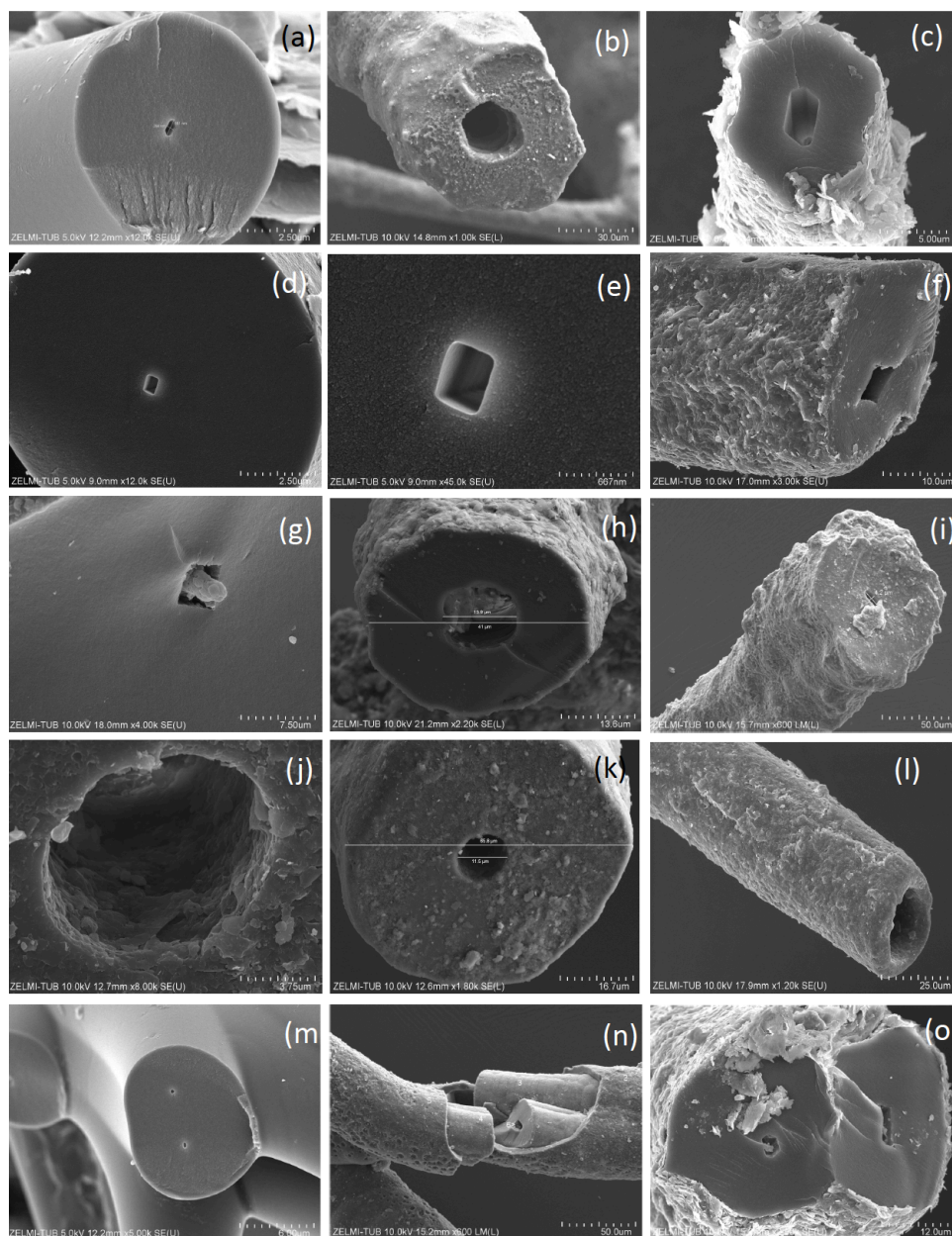
Fig. 11: SEM images of broken filamentous fossils, illustrating the central channel. (a,b,c) Six-sided channel in filament with (a) smooth outer surface, (b) dented surface, and (c) strongly mineralized surface. (d, e, f, g) Rectangular channel; (e) is enlarged part of (f). (h) Round, slightly irregular channel. (i) 4 μm x 6 μm wide channel on filament with dented surface. (j) Round channel, enlarged from (k), approximately 12 μm wide in a filament of nearly 70 μm diameter. (l) Slightly conical end of a filament with large, round channel. (m) Two filaments one with a small μm-wide channel attached to a hollow filament. (n) Channel in a filament with sheath-like structure. (o) Two filaments with six-sided channels.

393   A very characteristic feature of the filaments is a central channel (Fig. 11), observed in many

394   but not all of the filaments. The cross section of the channel can be six-sided (Fig. 11a-c,m),

395   rectangular (Fig. 11d-f), or round (Fig. 11h-l). The channel diameter is variable and ranges from

396   approximately 0.5 µm to 25 µm in filaments with an outer diameter between approximately 5

397   µm and 100 µm; examples in Fig. 11 show 5 µm with a channel of 260 nm x 550 nm (a), 50

398   µm with a channel of approximately 20 µm (b), 10 µm with a channel of 2.5 µm x 4 µm (c),

399   100 µm with a channel of 400 nm x 560 nm (d,e), 41µm with a channel of 14 µm (i).

400   4.3 Stable isotopes and C/N variation

401   Stable isotopes of C and N were obtained from all bulk samples (Table 1); it was not possible

402   to determine individual fossilized objects. In addition, we determined OM in black opal and

403   OM adherent to topaz (see sample list in Franz et al., 2022a).

404   Results of $\delta^{13}C$ and $\delta^{15}N$-determination and the molar C/N show a large variation (Fig. 12). All

405   $\delta^{13}C$ values are negative, and for kerite fossils vary between -47 (sample 2) and -31 ‰ (sample

406   1); $\delta^{15}N$ values vary between ~3 to 4 ‰ (samples kerite 0, 4) and ~10 ‰ (samples 1, 3). OM

407   associated with opal and topaz (considered as 'secondary') and buddingtonite, which obtained

408   its N from decayed OM, is less negative and homogeneous in $\delta^{13}C$ with values between -25

409   and -27 ‰. The C-values should be considered as maximum values, since alteration either by

410   deep-seated CO_2 from the mafic magmas or from meteoric waters would have increased $\delta^{13}C$.

411   The close group of $\delta^{13}C$ and $\delta^{15}N$ values for secondary OM indicates that during maturation

412   and decay they all have reached a similar value. The variation of the N-isotopes is not correlated

413   with the C-isotopes, and there is also no correlation with C/N.

414

415   Table 3 Results of $\delta^{15}N/^{14}N$, $\delta^{13}C/^{12}C$, and molar C/N of bulk kerite samples

Sample#	weight mg	δ $^{15}N/^{14}N$ ‰	mg N/sample	% N	δ $^{13}C/^{12}C$ ‰	mg C/sample	% C	molar C/N
1	2.76	9.99	0.038	1.37	-30.66	1.91	69.07	58.74
2	2.37	8.44	0.067	2.85	-46.99	0.63	26.52	10.87
3	2.21	10.23	0.027	1.20	-31.38	1.24	56.10	54.58
4	2.52	2.98	0.033	1.31	-33.61	0.44	17.34	15.48
5	4.01	7.37	0.096	2.38	-45.19	0.88	21.98	10.78
6	3.14	7.79	0.037	1.19	-44.06	0.27	8.55	8.39
7	4.29	6.87	0.074	1.73	-43.58	0.71	16.54	11.17
Opal 8	50.15	2.02	0.013	0.03	-25.32	0.55	1.09	49.23
Topaz 9	54.46	1.56	0.023	0.04	-25.73	0.38	0.69	18.89

416
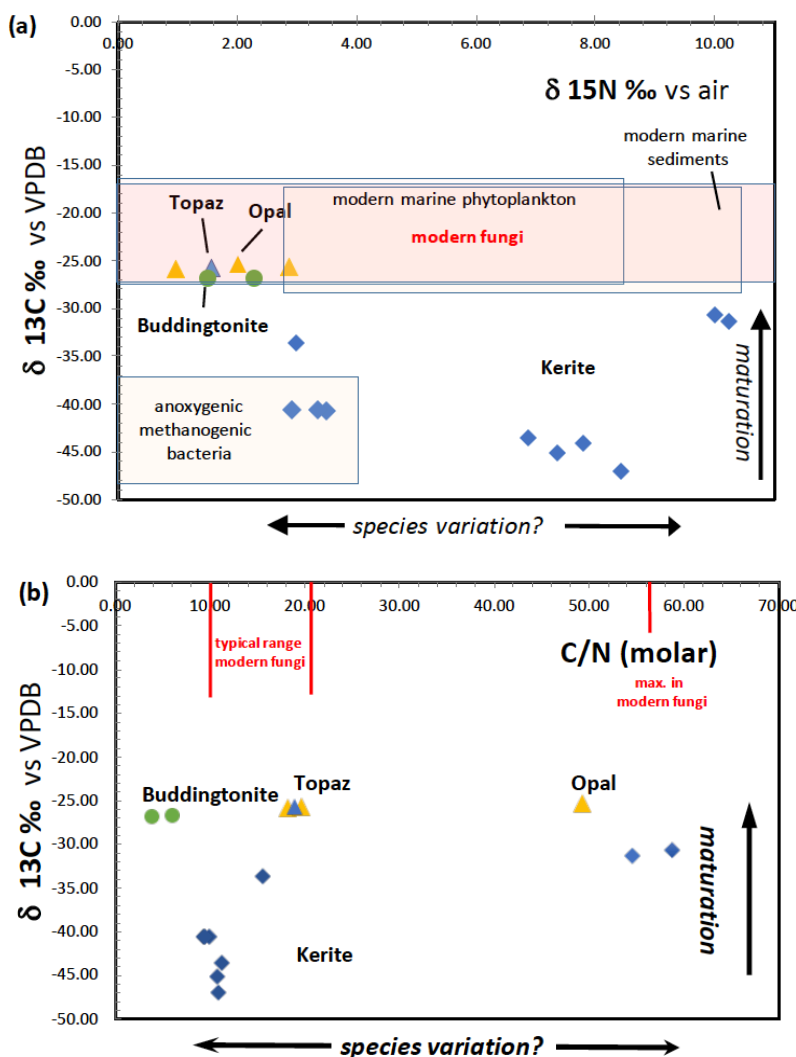
417

418
419 **Fig. 12: (a) Results of determination of δ13C and δ15N of Volyn biota and degraded kerite.**
420 **Symbols: Blue diamonds – dominantly filamentous kerite, with small amounts of flaky**
421 **and spherical OM; yellow triangle - black opal with OM; blue triangle - OM adherent to**
422 **topaz; green dots - buddingtonite from breccia (from Franz et al., 2017). Fields of modern**
423 **fungi from Mayor et al. (2009); modern marine sediments, phytoplankton and**
424 **methanogenic bacteria are summarized from Levin and Michener (2002), Peterson and**
425 **Fry (1987), Rau et al. (1990, 1996), and Struck (2012). (b) Molar C/N ratio of kerite fossils**
426 **and degraded OM. Range of C/N of modern fungi from Mayor et al. (2009).**

427 **4.4 FTIR investigation**

428 All measured FTIR spectra of morphologically different kerite fragments in the sample #0 are

429 very similar (Fig 13a) and resemble closely the chitosan spectrum (Fig 13b); both spectra are

430   dominated by two main groups of absorption bands located in the regions of 3500-2500

431   cm^{-1} and 1800-900 cm^{-1}. The first group consist of overlapping broad bands due to O-H and N-

432   H stretching vibrations, with a group of characteristic narrow peaks of C-H stretching vibrations

433   on their long-wavelength wing in the region of 2960-2870 cm^{-1} (Fig. 13; for detailed band

434   assignments and for spectra of chitin see Table 1 Supplement). The peak in vicinity of 1650

435   cm^{-1} is diagnostic of C=O group (Wanjun et al., 2005; Coates, 2011; Loron et al., 2019), the

436   band at 1560 cm^{-1} (broad shoulder near 1570 cm^{-1} in kerite spectra) was assigned to N-H

437
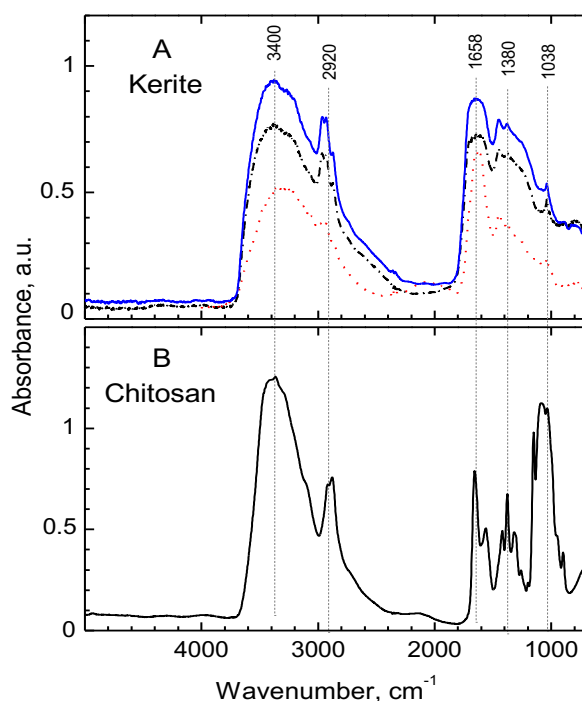
Fig. 13: FTIR spectra of filamentous fossil compared to standard materials chitin and
chitosan. (a) Complete spectra of three pieces of sample kerite #0, the sample with less
mineralization, showing two main regions of absorption: 3500 cm^{-1} to 2800 cm^{-1} and 1850
cm^{-1} to 900 cm^{-1}; (b) Standard material chitosan. Compared to chitosan the major
absorption bands in kerite spectra are broader, the weak shoulder near 3100 cm^{-1} in
chitosan spectrum is not present in kerite. The narrow triplet near 2950 cm^{-1} is observed
as doublet in chitosan, shifted to lower wavenumbers. In the part from 1800 cm^{-1} to 700
cm^{-1}, kerite shows only broad absorption, shifted towards higher wavenumbers compared
to chitosan, with three superimposed distinct weak peaks at 1450 cm^{-1}, 1380 and 1038 cm^{-1}
^{1}; the first is not present in chitosan, which has a number of distinct peaks in this region.

448 bending vibrations in amide group. The relatively weak band near 1420 cm^{-1} (1450 cm^{-1} in

449 kerite) was attributed to C-H bend (Loron et al., 2019), and the sharp peak at 1380 cm^{-1}, which

450 was reported in cellulose, chitosan, and chitin spectra, was assigned to superposition of O-H

451 bend (pyranose ring; Li et al., 2009) and symmetrical bend of CH$_3$ group. A band centered near

452 1315 cm^{-1} in chitin and chitosan spectra due to C-N stretching vibrations in amide group

453 (Vasilev et al., 2019; Wanjun et al., 2005) is not observed in kerite.

454 A broad, weak band at around 2100 cm^{-1} is present in spectra of kerite and chitosan (Fig. 13),

455 and the same type of weak bands are shown in published chitosan spectra (see Table 1

456 Supplement), but not mentioned and assigned. It can probably be attributed to overtone or

457 combination bands of pyranose ring vibrations. At lower wavenumbers, in all measured spectra

458 there is a series of strong (1150, 1180, 1030 cm^{-1}) and several weak bands caused by different

459 types of C-O vibrations in polysaccharides (Nakamoto, 1997; Wanjun et al., 2005; Li et al.,

460 2009; Coates, 2011; Loron et al., 2019; Vasilev et al., 2019).

461 A general observation is that in kerite spectra, compared to chitosan, all characteristic

462 absorption bands of the amide group and the pyranose ring become broader and weaker, in

463 agreement with earlier studies of spectroscopic changes during chitin/chitosan degradation

464 (Wanjun et al., 2005; Zawadzki and Kaczmarek; 2010; Vasilev et al., 2019). Nevertheless, the

465 main absorption features caused by amide group, diagnostic of chitosan, are still present in

466 kerite spectra.

467 **5 Discussion**

468 **5.1 Model for a Precambrian deep biosphere ecosystem**

469 The Volyn occurrence is a well-preserved example of a fossil ecosystem of the deep biosphere.

470 We exclude an a-biotic origin as previously postulated (Ginzburg et al., 1987; Lu'kyanova et

471 al., 1992) because of the extremely low δ^{13}C values and the large variation in morphology. In

472 combination with textural arguments, the age determination of muscovite, formed in

473 pseudomorphs after beryl, point to a minimum age of 1.5 Ga (Franz et al., 2022b); the maximum

474 age is restricted by the intrusion of the igneous rocks at 1.760 Ga (Shumlyanksyy et al., 2021.

475 The geological context argues for a continental, terrestrial environment, because the KPC

476 intruded into continental crust most likely in a within-plate tectonic setting (Shumlyanskyy et

477 al., 2012, 2017). After intrusion uplift to the erosion level occurred, documented by an

478 unconformity, and sedimentation started with sandstones and shales at approximately 1.4 Ga

479 (Zbranki Formation; Gorokov et al., 1981), later than or coeval with the pseudomorph

480 formation and the minimum age of the microfossils. The depth, where the organisms lived, is
481 an open question, but the occurrence in the underground mines indicate a depth of up to at least
482 150 m. The age of 1.5 Ga is much later than the oxygenation of the Earth's atmosphere allowing
483 the evolution of complex species and ecosystems on the land (sub)surface.

484 The Precambrian age clearly argues for fossils of microorganisms. The large size of the
485 filaments up to cm in length is a-typical for bacteria and archaea. However, Volland et al. (2022)
486 described recent cm-long bacteria, and the term 'microorganisms' in the original description
487 that they can be observed only on the microscopic scale, is not really appropriate. Putative cm-
488 sized Precambrian fossils (different from the Volyn biota) were reported from the 2.1 Ga old
489 Francevillian biota (El Albani et al., 2014); however, they are completely pyritized and occur
490 in diagenetically overprinted black shales, which makes the interpretation difficult.

5.2 Summary and interpretation of morphological and internal characteristics

492 The Volyn biota show an astonishingly large variation of different types of filaments and other
493 forms, pointing to the interpretation that different species were involved. We have already
494 interpreted the flaky objects of OM on the surface of beryl crystals (Fig. 2e,f) as biofilms (Franz
495 et al., 2022a). Agglutinated filaments (Fig. 6f) and the hollow object agglutinated to a filament
496 (Fig. 7i) can similarly be interpreted as fossilized biofilms. The sheath-structure (obvious e.g.
497 in Fig. 5i, j) is also an indication for the presence of a biofilm or extracellular polymeric
498 substances (EPS).

499 Some objects have a base onto which they grew (Figs. 3j-l, 8, 9a-c) and one object shows a
500 hollow lower part, from which bulbous outgrowths originate (Fig. 7a, b), pointing to sessile
501 organisms. Filaments are generally fragmented, but a few filaments have been found with two
502 intact ends (Figs. 4c, g, 6i, o), and we interpret this as either floating organisms or as an
503 indication for growth of organisms in a soft (possibly organic or clay mineral) substrate.

504 Thickness of the filaments varies from ≤10 µm to >200 µm. In filaments with diameter up to
505 approximately 30 µm, branching with thinning out of the branch clearly show that these are
506 within-species variations (irregular diameters of filaments, Fig. 2i, j, are interpreted as collapse
507 structures during fossilization). However, very thick filaments with diameters in the range of
508 ≥200 µm with a structured, bulbous surface (e.g. Fig. 6), or conical objects (Fig. 4m) are
509 interpreted as different species. The length of both types of filaments reaches the mm-range,
510 possibly up to cm-length.

511 Branching as indication for growth of the organisms is typical in the thin filaments, with Y-,
512 T-, double-T-, and multiple branching (Fig. 3), but anastomosing was not observed. In thick

513   filaments with diameter near 200 µm branching was not found. The ends of filaments also hint

514   to the type of growth. Simple round ends are rare, more typical are ball-shaped ends (Fig. 4).

515   Ball-shaped outgrowths along filaments are interpreted as beginning of a branching (Fig. 4h).

516   In the complete filaments (Fig. 4c, g) with one end thinning out, one with a ball-shaped end,

517   the thinning-out end is possibly the origin, the ball-shaped protrusions the growing end, because

518   ball-shaped ends are rather continuous in shape, from a small protrusion (Fig. 4b) to a more

519   complete ball (Fig. 4f, i). Similar protrusions were found at the end of recent, large bacterial

520   filaments (Volland et al., 2022). However, branched, thinning-out ends of the filaments (Fig.

521   3j-l, m) indicate ends similar to spitzenkörper, what in modern fungi is described as a

522   continuous and indefinite process of cell extension (Fischer et al., 2008).

523   Segmentation in thin filaments (Figs. 5m, 6g, h) with distances of a few µm up to tens of µm is

524   accentuated by mineralization (Fig. 5n), with irregular ridges caused by mineralization. Thick

525   filaments do not show a clear segmentation; the morphology is more irregular and shows

526   rounded, polygonal structures on the surface with dimensions of approximately 20-30 µm

527   (parallel to filament axis) x 35-70 µm (perpendicular to filament axis) (Figs. 5g, h, i, 6b, c).

528   Between the polygonal structures on the surface, remnants of a sheath are visible. In cross

529   section (Fig. 10) segmentation is clearly visible by cracks with a distance of approximately 50-

530   100 µm.

531   Bulbous forms (Figs. 7a, b, 8) mark the beginning of growth of some objects, and bulbous

532   outgrowths are very typical for thick filaments (Fig. 6, d, f), which extend into approximately

533   20 µm large objects, which consist of smaller bulbs (Fig. 6l, n). In thin filaments with typical

534   branching, the outgrowths are rare and more regularly ball-shaped (Figs. 3f, g, 4h), indicating

535   one species with prominent growth by branching of thin filaments, and another species with

536   growth by outgrowths along thick filaments.

537   Among the spherical objects, only the small ones with a size of a few µm (Fig. 9l-o) resemble

538   spores or other types of seeds/fruit bodies. The irregular, large objects several hundred µm in

539   size (Fig. 9d-k) do not fit into any scheme of known (micro)organisms. Similarly, there is no

540   obvious interpretation for the large bowl-shaped and irregular hollow objects (Fig. 8). The small

541   double-object with a partly preserved sheath (Fig. 9a-c) grown on a substrate has some

542   similarities with cell division.

543   The function of the conspicuous central channel (Fig. 11) in many, but not all filaments with

544   different shape in cross section is speculative, likely providing pathways for transport of

545   components for cell extension along the filament axis. In one example we observed a type of

546   filling in the channel (Fig. 11g), so in the original organisms it might have been filled with an

547   easily degradable substance. It is not clear if a hollow form (Fig. 7e, l) is a different phenomenon

548   or due to special preservation conditions. The width of the preserved rim is in the same order

549   of magnitude as the silicified rim (1-2 μm) and therefore it might just be a remnant of a filament,

550   in which the central part was completely degraded.

551   Another special feature of the internal structure are the nanometer-sized mineral inclusions of

552   Bi-S-Te minerals (Fig. 7). The organisms were able to concentrate these elements, either

553   irregularly distributed (Fig. 7c) or rod-like aligned (in a bulbous object; Fig. 7h). It is unclear if

554   the relatively large Bi-S mineral with some Cu and Fe contents in the center of a thick filament

555   (Fig. 7e) in the central channel is the original position of the Bi-S concentration or an effect of

556   fossilization. Modern fungi are able to concentrate Te (and Se) as nm-sized crystals (Liang et

557   al., 2020) and could be used in technology for soil mycoremediation (Liang et al., 2019). In

558   black shales, the organophilic element Bi might behave similar as Se (Budyak and Brukhanova,

559   2012). Biogeochemistry of Te is probably analogous to Se (Missen et al., 2020), but little is

560   known about the link of Bi to S and Te in OM (such as in coal, e.g. Finkelman et al., 2019).

561   The concentration of Bi-S-Te in the organisms of the Volyn biota is another indication for

562   fungi-like organisms, although other organisms are also able to concentrate Te (Missen et al.,

563   2020).

564   Remnants of cell membranes, separating individual cells, could not be identified, and to answer

565   the question if some of the organisms were multicellular is speculative. However, the large size

566   of many objects of the Volyn biota already indicates that possibly they were not single-celled

567   but multicellular, notwithstanding that single-cell bacteria (*Thiomargarita magnifica*; Volland

568   et al., 2022) can reach the size of cm. These macroscopic single-cell bacteria show a very simple

569   straight filament, whereas the large objects from the Volyn biota show a much more

570   complicated form; the surface of large filaments shows a bulbous structure with sizes in the

571   order of tens of μm (Figs. 5g-i, 6c, f, 9a, b), well visible with a polygonal network (Fig. 5j). In

572   the internal structure we also see phenomena that could be explained as separate cells, such as

573   the gaps in a filament (Fig. 10a) or in a bulbous object (Fig. 10g). The interior structure visible

574   in the element distribution of N (Fig. 7j) might indicate the original distribution in former

575   interior cell walls, in which chitin-like substance was concentrated. Finally, the small spherical

576   object shown in Fig. 9a, b might be taken as two cells, with an envelope of a sheath.

577

578

26

5.3 Stable isotopes

Modern fungi show a very wide variation of $\delta^{15}N$ from -5 ‰ to +25 ‰, with the main cluster between - 5 ‰ and +12 ‰, and $\delta^{13}C$ is restricted to -19 ‰ to -29 ‰ $\delta^{13}C$, with the main cluster at -22 ‰ to - 28 ‰ $\delta^{13}C$ (Mayor et al., 2009; Fig. 12a). Whereas the N-signature of kerite is consistent with the interpretation as fossil fungi, the C-signature is much lower than that of modern fungi. However, fungi live from consumption of organic matter, and this C-signature is transferred to the fungi. During consumption of C from modern plants to fungi, the $\delta^{13}C$-signature of -27 ‰ to -30 ‰ in plants changes to - 25 ‰ to -27.5 ‰ $\delta^{13}C$ in fungi (e.g. Högberg et al., 1999). Assuming that the isotope fractionation in the Volyn biota was similar, the consumed organism had a C-signature of c. -35 ‰ to -50 ‰ $\delta^{13}C$. These very low values are consistent with the interpretation that the primary organisms were anoxygenic/methanogenic bacteria. Another factor, which must be considered, is intracellular heterogeneity as observed in bacteria (Lepot et al., 2013). The membrane (lipids) can have a signature of 10 ‰ $\delta^{13}C$ lower than the bulk cell, and degradation during fossilization of the proteins and polysaccharides can lower the now determined C-signature. It is also possible that the fungi consumed biofilm. Fossil biofilms of the 2.75 Ga Hardey Formation (Australia), probably coexisting with methanogens, methanotrophs, and sulfur-metabolizing bacteria have $\delta^{13}C$ of -55 ‰ to -43 ‰ (Rasmussen et al., 2009), well in the range of $\delta^{13}C$-values observed here. The biofilms, described by Rasmussen et al. (2009), lived in synsedimentary cavities similar to stromatolites, pointing to the importance of cavities for the preservation of organic matter, similarly as the biofilms at Volyn in the deep biosphere.

Maturation clearly affects the C- and N-isotope ratios, which we see in degraded OM preserved in black opal, in OM adherent to topaz, and buddingtonite which obtained its NH_4 from OM. These samples have much more positive $\delta^{13}C$ and more homogeneous $\delta^{15}N$ values near +1.5 to +3 ‰ (Fig. 12a). In contrast, the large variation of $\delta^{15}N$ between 3 ‰ and 10 ‰ in the kerite fossil samples (Fig. 12a) and C/N between 10 and >50 (Fig. 12b) possibly indicates a variation of the species. These values were less influenced by maturation, as there is no correlation between $\delta^{13}C$ and C/N in all samples (fossils and degraded OM). Alleon et al. (2018) in their description of the 3.4 Ga old Strelley Pool microfossils (Western Australia) argued that though the fossils experienced heating up to 300 °C, the C/N did not change significantly. Also, for anthracite coal it has been shown that the original C/N did not vary with coalification (Anwita et al., 2020).

611   Loron et al. (2019) reported fossil fungi from the 1 Ga Grassy Bay Fm Canada, and provided

612   proof via chitin remnants (FTIR) and showing the characteristic bilayered fungal cell walls

613   (TEM data). However, the few SEM images for the Grassy Bay biota do not allow a comparison

614   with the Volyn biota. Following their discussion, the FTIR investigation of the filamentous

615   Volyn sample shows good indications for preserved chitosan as part of the OM. Degradation

616   studies of chitosan (Wanjun et al., 2005; Zawadzki and Kaczmarek; 2010; Vasilev et al., 2019)

617   showed that the spectra of kerite has the same characteristic bands as chitosan at approximately

618   250 °C; at lower as well as at higher temperatures these bands disappear. Completely

619   independent temperature estimates for the fossilization based on phase equilibria of Be minerals

620   yielded the same temperature range (Franz et al., 2017).

621   **5.4 Taxonomy and comparison with Precambrian biota**

622   Film-like microfossils were described from the 3.4 Ga old Strelley Pool (Western Australia;

623   Alleon et al., 2018), the 3.3-3.5 Ga old Onverwacht Group (Australia; Westall et al., 2001),

624   from the 2.75 Ga old Hardey Formation (Australia; Rasmussen et al., 2009) and there is little

625   doubt that biofilms existed for a long time in the Earth's history and are an integral component

626   of the ancient life cyle (Hall-Stoodley et al., 2004). It seems safe to assume that the irregular

627   (Fig. 2f, and images in Franz et al., 2022a) and sheath-like structures (Figs. 5i,j, 6f, 9a) of the

628   Volyn biota were biofilms.

629   We have already pointed out that some of the organisms show analogies to fungi. Based on the

630   molecular clock technique, Wang et al. (1999) estimated the divergence between the three-way

631   split of the kingdoms animals-plants-fungi at 1.58±9 Ma, much earlier than the 'Precambrian

632   explosion'. This age is in the same range as the minimum age of the Volyn biota. Other

633   molecular clock estimates indicate that the first zygomycetous fungi occurred on Earth during

634   the Precambrian, approximately 1.2–1.4 Ga ago (review in Krings et al., 2013). Diversification

635   of fungi and transition to land was dated at ca. 720 Ma (Lutzoni et al., 2018) and they estimate

636   the origin of fungi at ca. 1240 Ma, similarly as Berbee et al. (2020), who placed the origin of

637   fungi at ca. 1300 Ma. If indeed the Volyn biota contain fungi-like organisms, their origin as

638   well as colonization of land occurred earlier than ca. 1500 Ma.

639   Bengtson et al. (2017) reported fungus-like organisms from the deep biosphere, which are from

640   the 2.4 Ga Ongeluk Formation (South Africa), however not terrestrial but marine. The

641   important fact is that these fossils were found also in open cavities, though of a completely

642   different size, mm-amygdales in low-grade metamorphic basalt, in contrast to the huge cavities

643   of tens of meter size in the pegmatites from Volyn. The filaments from the Ongeluk biota with

644   a diameter of ca. 2 µm to 12 µm are generally thinner than the Volyn biota and show
645   anastomosis, but also Y- and T-branching, and sometimes bulbous protrusions, 5-10 µm in
646   diameter. A special feature is what Bengtson et al. (2017) call 'broom structure', diverging
647   filaments growing from a substrate of clay minerals (chlorite), and the filaments consist also of
648   the same type of chlorite. These structures (shown in 2D in thin sections) could be similar as
649   the object from the Volyn biota (Fig. 3j, k, l), and what we called 'multiple branching' (Fig. 3c,
650   e, g). A significant difference between the two biota is the fossilization process, which resulted
651   in the Ongeluk biota in complete replacement of the filaments by clay minerals, whereas at
652   Volyn fossilization is restricted to the outermost rim and most of the C is preserved (Franz et
653   al., 2022a).

654   Good evidence for fungi-like organisms were reported from the early Ediacaran Doushantuo
655   biota, at approximately 635 Ma (Gan et al., 2021). These fossils are pyritized, but with remnants
656   of organic matter, and consist of branching filaments (Y-, T-branching, but also with A- and H-
657   type and anastomosis) and associated hollow spheres. Compared to the Volyn biota, the
658   filaments are thinner (two types, one with average 6.8 µm, one with average 2.7 µm), whereas
659   the observable length in thin section with hundreds of µm is possibly in the same range as in
660   the Volyn biota. The spheres of the Doushantuo biota are hollow and coaxially aligned, but also
661   similar to what we described as ball-shaped outgrowths; their size varies from average 16 µm
662   to 20 µm in small ones and large spheres with 36 µm to 102 µm, similarly to the Volyn biota
663   (Fig. 4h, i for the small spheres, Fig. 4j for large spheres). The fact that the spheres of the
664   Doushantuo Formation are hollow is possibly due to the fact that they are mostly pyritized, i.e.
665   most of the organic matter was decomposed. The small spheres were interpreted (Gan et al.,
666   2021) as possible spores, the larger ones were possibly symbiontic organisms living together
667   with the fungi.

668   Other possible organisms are palynomorphs, which are among the earliest clear records of
669   terrestrial life (Wellman and Strother, 2015), described from the ca. 1.08 Ga old Nunsuch Shale
670   of the Oronto Group (Michigan). This microbiota shows cell clusters, with little similarity to
671   morphologies of the Volyn biota. However, the Nunsuch biota come from a surface
672   environment, whereas the Volyn biota from the deep biosphere. We do not see similarity with
673   the 1.67 Ga eukaryotic Changcheng biota (Miao et al., 2019) or with vase-shaped metazoan
674   microfossils, considered as the oldest evidence for heterotrophic protists (e.g. Urucum
675   Formation, Brazil; Morais et al., 2017).

676 Most of the Precambrian biota listed in the literature are considered as photosynthetic
677 organisms, probably not a likely analog for the Volyn biota. E. g. the 770 Ma (Cryogenian)
678 Chichkan Fm. in Maly Karataou, Kazakhstan (Sergeev and Schopf, 2010) contains biota in
679 fine-grained black chert, which were deposited in a mid-shelf and a near-shore environment
680 with stromatolites. Most of the biota listed by Sergeev and Schopf (2010) are cyanobacteria,
681 rather small mostly up to the 10 µm range and thus do not serve as analogues for the Volyn
682 biota. They also list a number of larger protista (*incertae sedis*) in the 100 µm-range, however
683 with little morphological similarity to the Volyn biota. No similarity was found to eukaryotes
684 (acryitarchs) from 1.1 Ga old Taoudeni basin, Mauretania (Beghin et al., 2017). Red algae
685 (rhodophytae) from the 1.05 Ga Hunting Fm, considered as the oldest eukaryotes (Butterfield,
686 2000; Gibson et al., 2018) are photosynthetic organisms and can also be excluded.

687 **6 Summary and conclusions**

688 The exceptional 3D preservation of the 1.5 Ga Volyn biota is due to the fossilization conditions
689 in open cavities, with SiF_4-rich fluids as the driving agent. There are a number of indications
690 that fungi-like organisms were likely an important part of the microecosystem – hyphen with
691 branching (though not anastomosing), growth in thinning-out ends, and also in bulbous
692 extrusion, both at the end of filaments and along the filaments. Sheath-like structures are clearly
693 visible, and there are good indications for a former biofilm and extracellular proteinic
694 substance. The large size and internal structure of the organisms and the segmentation visible
695 on thick filaments points to multicellular organisms, and the nano-sized inclusions of Bi(S,Te)
696 crystals have an astonishingly good analog in recent fungi. The stable N- and C-isotopic
697 signature is in accordance with such an interpretation.

698 The fungi-like organisms possibly lived from lithotrophic methanogenic bacteria; alternatively
699 or additionally bacteria such as cyanobacteria were transported from the surface downwards
700 into the cavities. The geyser system of the Korosten Pluton provided an ideal framework for
701 growth of bacterial or algal organisms at the surface. In the deep biosphere, benthic forms of
702 the organisms are observed as well as organisms floating in water or growing in soft clay media,
703 but not attached to the clay.

704 The Volyn biota show that fungi-like organisms developed before 1 Ga (Loron et al.; 2019),
705 and support the speculation that the fossils from the 2.4 Ga Ongeluk Formation were fungi-like
706 organisms (Bengtson et al., 2017). Molecular clock data, especially the three-way split of the
707 kingdoms animals-plants-fungi at 1.58±9 Ma (Wang et al., 1999) are still uncertain, but our
708 data indicate that it must have occurred early in the Proterozoic.

709   The Volyn biota also prove that a deep continental biosphere was already present in the Early

710   Mesoproterozoic/Late Paleoproterozoic. It is known that in the subseafloor environment

711   microbial life existed in the Archean (Cavalazzi et al., 2021), as described from the 3.4 Ga old

712   Onverwacht Group of the Barberton greenstone belt, but from the continental environment this

713   has not yet been reported. Furthermore, the Volyn biota must have been highly radiation

714   resistant (e.g. the bacteria *Deinococcus radiodurans* or *Thermococcus gammatolerans*; see

715   review in Matusiak, 2019), because a U-Th-K-rich granitic-pegmatitic system has a high

716   radiation level. During the mining operations in Soviet times, a high Rn content was measured

717   inside cavities, when they were broken into. The general radiation levels, 3000 times higher

718   than the allowed limit at that time, were even higher 1.5 billion years ago. Deeply black-colored

719   quartz crystals in the pegmatites are of the 'morion' type and also indicate high radiation.

720   Recent observations at the Tschernobyl power plant have led to the speculation about

721   radiotrophic fungi (e.g. Matusiak, 2019; Prothmann and Zauner, 2014), which produce melanin

722   as a protection against radiation and enhancement of fungal growth via capture of ionizing

723   radiation for energy conversion (Dadachova et al., 2007; Tugay et al., 2017). Mycoremediation

724   is at least a well-documented mechanism for a very effective method of radio nuclides pollutant

725   removal considering the versatility of fungi in terms of their ecology, nutritional modes,

726   adaptability, morphology, physiology, and metabolism (Shourie and Vijayalakshmi, 2022).

727   Fungi are known as extremophylic organisms (e.g. Blachowicz et al., 2019) and we can expect

728   that in the Proterozoic or possibly already earlier in Earth history similar organisms were active

729   and resistant to a high radiation level, in an epoch when the ozone layer was not yet fully

730   developed.

731

732

738

739   **Author contribution**

740   Concept, writing, interpretation, EMPA and SEM data acquisition - GF; IR spectra, writing -

741   VK; sampling - VC, PL; stable isotopes - US; SEM - UG; EMPA - JN.

742

References

Alleon, J., Bernard, S., Le Guillou, C., Beyssac, O., Sugitani, K., and Robert, F.; Chemical nature of the 3.4 Ga Strelley Pool microfossils, Geochem. Persp. Lett., 7, 37-42, 2018. doi 107185/geochemlet.1817.

Anwita, Gosh, S., Varma A. K., Das, S. K., Pal, D., and Solanki, G () Metamorphic tranformations of nitrogen functionalities: Stabilization of organic nitrogen in anthracite and its effect on $\delta^{15}N$ parameter, Marine Petrol. Geol., 112, 2020, doi.org/10.1016/j.marpetgeo.2019.104090.

Beghin, J., Storme, J.-Y., Blanpied, C., Gueneli, N., Brocks, J. J., Poulton, S. W., and Javaux, E. J.: Microfossils from the late Mesoproterozoic – early Neoproterozoic Atar/El Mreiti Group, Taudeni basin, Mauretania, northwestern Africa, Prec. Res. 291, 63-82, 2017.

Bengtson, S., Rasmussen, B., Ivarsson, M., Muhling, J., Broman, C., Marone, F., Stampanomi, M., and Bekker, A.: Fungus-like mycelial fossils in 2.4 billion-year-old vesicular basalt, Nature Ecol. Evol., 1(6), 1-6, 2017.

Berbee, M. L., Strullu-Derrien, C., Delaux, P.-M., Strother, P. K., Kenrick, P., Selosse, M.-A., and Taylor, J. W.: Genomic and fossil windows into the secret lives of the most ancient fungi, Nature Rev. Microbiol., 18, 717–730, 2020.

Blachowicz, A, Chiang, A. J., Elsaesser, A., Kalkum, M., Ehrenfreund, P., Totok, T., Wang, C. C. C., and Venkateswaran, K.: Protemoic and mteabolic characteristics of extremophilic fungi under simulated Mars conditions, Front. Microbiol. 10:1013, 2019, doi: 10.3389/fmicb.2019.01013

Budyak, A. E., and Brukhanova, N. N.: Selenium, bismuth, and mercury in black shale-hosted gold deposits of different genetic types, Geochem. Int., 50, 791-797, 2012.

Butterfield, N. J.: Bangiomorpha pubescens n. Gen., n. sp.: Implications for the evolution of sec, multicellularity, and the Mesoproterozoic/Neoproterozoic radiation of the eukaryotes, Paleobiol., 26, 386-404, 2000.

Cavalazzi, B., Lemelle, L., Siminovici, A., Cady, S. L., Russell, M. J., Bailo, E., Canteri, R., Enrico, E., Manceau, A., Maris, A., Salomé, M., Thomassot, E., Bouden, N., Tucoulou, R., and Hofman, A.: Cellular remains in a ~3.42-billion-year-old subseafloor hydrothermal environment, Sci. Adv., 7, eabf3963, 2021.

Coates J.: Interpretation of infrared spectra, a practical approach, Encyclopedia of Analytical Chemistry R.A. Meyers (Ed.), copyright John Wiley & Sons Ltd., 2011.

Dadachova, E., Bryan, R. A., Huang, X., Moadel, T., Schweitzer, A. D., Aisen, P., Nosanchuck, J. D., and Casedevall, A.: Ionization radiation changes the electronic properties of melanin and enhances the growth of melanized fungi, PLoS ONE, 5, 1-13, 2007.

El Albani, A., Bengtson, S., Canfield, D. E., Riboulleau, Bard, C. R., et al.: The 2.1 Ga old Francevillian biota: Biogenecity, taphonomy and biodiversity, PLoS ONE 9(6): e99438, 2014. doi: 10.1371/journal.pone.0099438.

Finkelman, R. B., Dai, S., and French, D.: The importance of minerals in coal as the hosts of chemical elements: A review, Int. J. Coal Geology, 212, 103251, 2019.

Fischer, R., Zekert, N., and Takeshita, N.: Polarized growth in fungi – interplay between the cycloskeleton, positional markers and membrane domains, Molec. Microbiol., 68, 813-826, 2008.

Franz, G. Khomenko, V. Vishnyevskyy, A. Wirth, R. Nissen, J. Rocholl A.: Biologically mediated crystallization of buddingtonite in the Paleoproterozoic: Organic-igneous interactions from the Volyn pegmatite, Ukraine, Amer. Mineral. 102, 2119-2135, 2017.

Franz, G., Lyckberg, P., Khomenko, V., Chournousenko, V., Schulz, H.-M., Mahlstedt, N., Wirth, R., Glodny, J., Gernert, U., and Nissen, N.: Fossilization of Precambrian organic matter (kerite) from the Volyn pegmatite, Ukraine, BioGeosci., 19, 1795-1811, 2022a.

792 Franz, G., Sudo, M., Khomenko, V.: $^{40}Ar/^{39}Ar$ dating of a hydrothermal pegmatitic
793 buddingtonite-muscovite assemblage from Volyn, Ukraine, Eur. J. Mineral., 34, 7-18, 2022b.
794 doi.org/10.5194/ejm-34-7-2022.
795 Gan, T., Luo, T., Pang, K., Zhou, Ch., Zhou, G., Wan, B., Li, G., Yi, Q., Czaja, A. D. and Xiao,
796 S.:Cryptic terrestrial fungus-like fossils of the early Ediacaran Period, Nature Comm.,
797 doi.org/10.1038/s41467-021-20975-1, 2021.
798 Gibson, T. M., Shih, P. M., Cumming, V. M., Fischer, W. W., Crockford, P. W., Hdgekiss, M.
799 S. W., Wörndle, S., Creaser, R. A., Rainbird, R. H., Skulski, T. M., and Halverson, G. P.:
800 Precise age of Bangiomorpha pubescens dates the origin of eurkaryotic photosynthesis,
801 Geology, 46, 135-138, 2018.
802 Ginzburg, A.I., Bulgakov, V.S., Vasilishin, I.S., Luk'yanova, V.T., Solntseva, L.S., Urmenova,
803 A.M., and Uspenskaya, V.A.: Kerite from pegmatites of Volyn, Dokl. Akad. Nauk SSSR, 292,
804 188–191, 1987, (in Russian).
805 Gorlenko, V.M., Zhmur, S.I., Duda, V.I., Osipov, G.A., Suzina, N.E., and Dmitriev, V. V.: Fine
806 structure of fossilized bacteria in Volyn kerite, Orig. Life Evol. Biosph., 30, 567–577, 2000.
807 Gorokov, I. M., Clauer, N., Varshavskaya, E. S., Kutyavin, E. P., and Drannik, A. S.: Rb-Sr
808 ages of Precambrian sediments from the Ovruch Mountain range, Northwestern Ukraine
809 (U.S.S.R.), Precam. Res., 6, 55-65, 1981.
810 Hall-Stoodley, L., Costerton, J. W., and Stoodley, P.: Bacterial biofilms: From the natural
811 environment to infectious diseases, Nature Rev. Microbiol., 2, 95-108, 2004.
812 Högberg, P., Plamboeck, A. H., Taylor, A. F. S., and Fransson, P. M. A.: Natural ^{13}C abundance
813 reveals trophic status of fungi and host-origin of carbon in mycorrhizal fungi in mixed forests,
814 Proc. Natl. Acad. Sci. USA, 96, 8534-8539, 1999.
815 Ivanovich, P. V., and Alekseevich, D. S.: Mineralogy of the Volynian chamber pegmatites,
816 EKOST Association, Mineral. Almanac, 12, 128 p, Moscow, 2007.
817 Krings, M., Taylor, T. N., and Dotzler, N.: Fossil evidence of the zygomycetous fungi,
818 Persoonia, 30, 1-10, 2013.
819 Lepot, K., Williford, K. H., Ushikubo, T., Sugitani, K., Mimura, K., Spicuzza, M. J., and
820 Valley, J. W.:Texture-specific isotopic compositions in 3.4 Gyr old organic matter support
821 selective preservation in cell-like structures, Geochim. Cosmochim. Acta, 112, 66-86, 2013.
822 Levin, L.A., and Michener, R.:Isotopic evidence of chemosynthesis-based nutrition of
823 macrobenthos: The lightness of being at Pacific methane seeps, Limnol. Oceanogr., 47, 1336-
824 1345, 2002.
825 Li J., Zhang L.-P., Peng F., Bian J., Yuan T.-Q., Xu F., Sun R.-C.: Microwave-assisted solvent-
826 free acetylation of cellulose with acetic anhydride in the presence of iodine as a catalyst,
827 Molecules, 14, 3551-3566, 2009. doi:10.3390/molecules14093551.
828 Liang, X., Perez, M. A. M.-J., Nwoko, K. C., Egbers, P., Feldmann, J., Csentenyi, L., and Gadd,
829 G. M.: Fungal formation of selenium and tellurium nanopartikels, Appl. Microbiol. Biotechn.,
830 103, 7241-7259, 2019.
831 Liang, X., Perez, M. A. M.-J., Zhang, S., Song, W., Armstrong, J. G., Bullock, L. A., Feldmann,
832 J., Parnell, J., Csentyi, L., and Gadd, G. M.: Fungal transformation of selenium and tellurium
833 located in a volcanogenic sulfide deposit, Environ. Microbiol., 22, 2346-2364, 2020.
834 Loron, C. C., François, C., Rainbird, R. H., Turner, E. C., Borensztajn, S., and Javaux, E. J.:
835 Early fungi from the Proterozoic era in Arctic Canada, Nature, 570.7760: 232-235, 1992.
836 Lu'kyanova, V. T., Lobzova, R. V., and Popov, V. T.: Filaceous kerite in pegmatites of Volyn,
837 Izvestiya Ross. Akad. Nauk Ser. Geologicheskaya, 5, 102-118 (in Russian), 1002.
838 Lutzoni, François, Michael D. Nowak, Michael E. Alfaro, Valérie Reeb, Jolanta
839 Miadlikowska, Michael Krug, A. Elizabeth Arnold et al.: Contemporaneous radiations of
840 fungi and plants linked to symbiosis, Nature Comm. 9, no. 1, 1-11, 2018.
841 Lyckberg, P., Chornousenko, V., and Wilson, W. E.: Famous mineral localities: Volodarsk-
842 Volynski, Zhitomir Oblast, Ukraine, The Mineral. Record, 40, 473-506, 2009.

843   Lyckberg, P., Chournousenko, V., and Chournousenko, O.: Giant heliodor and topaz pockets
844   of the Volodarsk chamber pegmatites, Korosten pluton, Ukraine, 36th Intern. Gemm. Conf.,
845   Nantes, France, Abstr. vol., 78-83, 2019.
846   Mariotti, A.: Atmospheric nitrogen is a reliable standard for natural ^{15}N abundance
847   measurements, Nature, 303(5919), 685-687, 1983.
848   Mayor, J. R., Schuur, E. A. G., and Henkel, T. W.: Elucidating the nutritional dynamics of fungi
849   using stable isotopes, Ecology Lett., 12, 171-183, 2009.
850   Matusyak, D. M.: Radiotolerant microorganisms – characterization of selected species and their
851   potential usage, Adv. Microbiol., 55, 182-194, 2016.
852   Miao, L. Y., Moczydłowska, M., Zhu, S. X. and Zhu, M. Y.: New record of organic- walled,
853   morphologically distinct microfossils from the late Paleoproterozoic Changcheng Group in
854   the Yanshan Range, North China, Precam. Res., 321, 172–198, 2019.
855   Missen, O. P., Ram, R., Mills, S. J., Etschmann, B., Reith, F., Shuster, J., Smith, D., J., and
856   Brugger, J.: Love is in the Earth: A review of tellurium (bio)geochemistry in surface
857   environments, Earth Sci. Rev., 2020, doi.org/10.1016/j.earscirev.2020.103150.
858   Morais, L., Fairchild, T. R., Lahr, D. J. G., Rudnitzki, I. D., Schopf, J. W., Garcia, A. K.,
859   Kudryavtsev, A. B., and Romero, G. R.: Carbonaceous and siliceous Neoproterozoic vase-
860   shaped microfossils (Urucum Formation, Brazil) and the question of early protistan
861   biomineralization, J. Paleontol., 91(3), 393-406, 2017. doi: 10.1017/jpa.2017.16.
862   Nakamoto K.: Infrared spectra of inorganic and coordination compounds, Parts A and B. New
863   York: Wiley, p. 328., John Wiley & Sons, New York, 1997.
864   Peterson, B.J., and Fry, B.: Stable isotopes in ecosystem studies, Ann. Rev. Ecol. Syst., 18,
865   293–320, 1987.
866   Prothman, C., and Zauner, K.-P. Semibiotic Persistence, J. Brit. Interplanet. Soc. (JBIS),
867   67(7-9), 314-321, 2014 doi://www.jbis.org.uk/paper.php?p=2014.67.314.
868   Rasmussen, B., Blake, T. S., Fletcher, I. R., and Kilbum, M. R.: Evidence for microbial life in
869   synsedimentary cavities from 2.75 Ga terrestrial environments, Geology, 37, 423-426, 2009.
870   Rau, G. H., Teyssie, J. L., Tassoulzadegan, R., and Rowler, S. W.: ^{13}C/^{12}C and., ^{15}N/^{14}N
871   variations among size-fractionated marine particles: implication for their origin and trophic
872   relationships, Marine Ecol. Progr. Ser., 59, 33–38, 1990.
873   Rau, G. H., Riebesell, U., and Wolf-Gladrow, D. A.: A model of photosynthetic ^{13}C
874   fractionation by marine phytoplankton based on diffusive molecular CO_2 uptake, Marine Ecol.
875   Progr. Ser., 133, 275–285, 1996.
876   Sergeev, V. N., and Schopf, J. W.: Taxonomy, paleoecology and biostratigraphy of the Late
877   Neoproterozoic Chichkan microbiota of South Kazakhstan: The marine biosphere on the eve of
878   metazoan radiation, J Paleont., 84, 363-401, 2010
879   Shourie, A., and Vijayalakshmi U.: Fungal diversity and its role in mycoremediation,
880   Geomicrobiol. J., 39, 3-5, 426-444, 2022, doi: 10.1080/01490451.2022.2032883
881   Shumlyanskyy, L., Billström, K., Hawkesworth, C., and Elming, S.-Å.: U-Pb age and Hf
882   isotope compositions of zircons from the north-western region of the Ukranian shield: mantle
883   melting in response to post-collision extension. Terra Nova 24, 373-379, 2012.
884   Shumlyanskyy L., Hawkesworth C., Billström K., Bogdanova S., Mytrokhyn O., Romer R.,
885   Dhuime B., Claesson S., Ernst R., Whitehouse M., Bilan O.: The origin of the Palaeoproterozoic
886   AMCG complexes in the Ukrainian Shield: new U-Pb ages and Hf isotopes in zircon, Precam.
887   Res., 292, 216-239, 2017.
888   Shumlyanskyy, L., Franz, G., Glynn, S., Mytrokhyn, O., Voznyak, D., and Bilan O.:
889   Geochronology of granites of the western part of the Korosten AMCG complex (Ukrainian
890   Shield): implications for the emplacement history and origin of miarolitic pegmatites, Eur. J.
891   Min., 33, 703-716, 2021.
892   Struck, U.: On the use of stable nitrogen isotopes in present and past anoxic environments. In:
893   Altenbach, A. V., Bernard, J. M. and Seckbach, J. (eds.) Anoxia, evidence for eukaryote

894   survival and paleontological strategies. Book series: Cellular origin, life in extreme habitats and
895   astrobiology, 21, 497-513, Springer, Berlin, 2012.
896   Tugay, T., Zhdanova, N.N., Zheltonozhsky, V., Sadovnikov, L., and Dighton, J.: The influence
897   of ionizing radiation on spore germination and emergent hyphal growth response reactions of
898   microfungi, Mycologia, 98, 4, 521-527, 2006/2017. doi: 10.1080/15572536.2006.11832654.
899   Vasilev, A., Efimov, M., Bondarenko, G., Kozlov, V., Dzidziguri, E., and Karpacheva, G.:
900   Thermal behavior of chitosan as a carbon material precursor under IR radiation, IOP Conf. Ser.:
901   Mater. Sci. Eng. 693, 2019, https://doi.org/10.1088/1757-899X/693/1/012002.
902   Volland, J.-M., Gonzalez-Rizzo, S., Gros, O., Tyml, T., Ivanova, N., Schulz, F., Goudeau, D.
903   et al.: A centimeter-long bacterium with DNA contained in metabolically active, membrane-
904   bound organelles. Science, 376.6600, 1453-1458, 2022. doi: 10.1126/science.abb3634.
905   Wanjun T., Cunxin W., Donghua, C.: Kinetic studies on the pyrolysis of chitin and chitosan,
906   Polym. Degrad. Stabil. 87, 389–394, 2005.
907   Wang, D. Y.-C., Kumar, S., and Hedges, S. B.: Divergence time estimates for the early history
908   of animal phyla and the origin of plants, animals and fungi, Proc. R. Soc. Lond., 266, 163-171,
909   1999.
910   Wellman, C. H., and Strother, P. K.: The terrestrial biota prior to the origin of land plants
911   (embryophytes): A review of the evidence, Paleontol., 58, 601-627, 2015.
912   Westall, F., de Witt, M. J., Dann, J., van der Gaast, S. de Ronde, C. E.J., and Gerneke, D.: Early
913   Archean fossil bacteria and biofilms in hydrothermally-influenced sediments from the
914   Barberton greenstone belt, South Africa. Prec. Res., 106, 93-116, 2001.
915   Zawadzki, J., and Kaczmarek, H.: Thermal treatment of chitosan in various conditions,
916   Carbohydr. Polym., 80, 394-400, 2010.
917   Zhmur, S. I.: Origin of Cambrian fibrous kerites of the Volyn region, Lithol. Mineral Resour.,
918   38, 55-73, 2003.